



# A unified determinant-preserving formulation for compressible/incompressible finite viscoelasticity

Ignasius P.A. Wijaya, Oscar Lopez-Pamies, Arif Masud \*

Department of Civil and Environmental Engineering, University of Illinois, Urbana-Champaign, IL 61801, USA

## ARTICLE INFO

### Keywords:

Elastomers  
Finite deformations  
Stabilized finite elements  
Stable ODE solvers

## ABSTRACT

This paper presents a formulation alongside a numerical solution algorithm to describe the mechanical response of bodies made of a large class of viscoelastic materials undergoing arbitrary quasistatic finite deformations. With the objective of having a unified formulation that applies to a wide range of highly compressible, nearly incompressible, and fully incompressible soft organic materials in a numerically tractable manner, the viscoelasticity is described within a Lagrangian setting by a two-potential mixed formulation. In this formulation, the deformation field, a pressure field that ensues from a Legendre transform, and an internal variable of state  $\mathbf{F}^v$  that describes the viscous part of the deformation are the independent fields. Consistent with the experimental evidence that viscous deformation is a volume-preserving process, the internal variable  $\mathbf{F}^v$  is required to satisfy the constraint  $\det \mathbf{F}^v = 1$ . To solve the resulting initial-boundary-value problem, a numerical solution algorithm is proposed that is based on a finite-element (FE) discretization of space and a finite-difference discretization of time. Specifically, a Variational Multiscale FE method is employed that allows for an arbitrary combination of shape functions for the deformation and pressure fields. To deal with the challenging non-convex constraint  $\det \mathbf{F}^v = 1$ , a new time integration scheme is introduced that allows to convert any explicit or implicit scheme of choice into a stable scheme that preserves the constraint  $\det \mathbf{F}^v = 1$  identically. A series of test cases is presented that showcase the capabilities of the proposed formulation.

## 1. Introduction

Viscoelastic constitutive models are an essential tool to advance the understanding of the mechanics of polymers, hydrogels, soft biological tissues, and any other soft organic material (Oyen and Cook, 2003; Eleni et al., 2013; Freed and Rajagopal, 2016; Mao et al., 2017; Budday et al., 2017; Ghosh et al., 2021). At continuum length scales, there are in effect two different classes of viscoelastic constitutive models that have been pursued in the literature. The first is based on hereditary-type integral representations of the stress and/or strain measures (Green and Rivlin, 1957; Pipkin and Rogers, 1968; Lockett, 1972). The second class, on the other hand, utilizes internal variables — defined via ordinary differential equations in time — to capture time dependence (Sidoroff, 1974; Le Tallec et al., 1993; Reese and Govindjee, 1998; Bergstrom and Boyce, 1998; Kumar and Lopez-Pamies, 2016). Because of their superior numerical tractability, models within the latter class have emerged as the preferred models of choice for applications. In this work, we focus on internal-variable-based viscoelastic models and, in particular, models that can be derived from the so-called two-potential framework (Halphen and Nguyen, 1975; Ziegler and Wehrli, 1987; Kumar and Lopez-Pamies, 2016). These are characterized by two thermodynamic potentials, a free-energy function that serves to characterize how the material stores energy

\* Corresponding author.

E-mail addresses: [iwijaya2@illinois.edu](mailto:iwijaya2@illinois.edu) (I.P.A. Wijaya), [pamies@illinois.edu](mailto:pamies@illinois.edu) (O. Lopez-Pamies), [amasud@illinois.edu](mailto:amasud@illinois.edu) (A. Masud).

through elastic deformation and a dissipation potential that serves to characterize how the material dissipates energy through viscous deformation. A distinct advantage of this approach is that it allows to enforce material frame indifference, material symmetry, and entropy imbalance from the outset in a straightforward manner (Kumar and Lopez-Pamies, 2016).

An important — yet often overlooked — consideration in the modeling of viscoelastic materials is the characterization of their compressibility. The vast majority of viscoelastic models available in the literature assume full incompressibility of the viscosity, while the elasticity is taken to be either compressible or fully incompressible; this is true not only for viscoelastic solids but also for viscoelastic fluids (Kwack and Masud, 2010; Anand et al., 2013; Kwack et al., 2017). In reality, no soft organic material — or any other type of material for that matter — is fully incompressible and some, actually, can feature a wide range of compressibilities depending on their fabrication process; see, e.g., Weir (1951), Hosseini-Farid et al. (2019) and Birzle and Wall (2019), Shrimali et al. (2021). As two prominent examples, we note for instance that the initial bulk-to-shear-modulus ratio of natural rubber has been measured to be in the order of  $10^4$  (Wood and Martin, 1964), while the bulk-to-shear-modulus ratio of closed-cell elastomeric and syntactic foams can range from (the very compressible)  $10^0$  to (the nearly incompressible)  $10^3$  depending on the content of porosity and microballoons (Idiart and Lopez-Pamies, 2012; Croom et al., 2019). These basic examples make it plain that accounting for the entire compressibility spectrum may be essential, especially in applications leading to localized regions of confining pressure.

In this context, the first of two objectives of this paper is to introduce a unified and numerically tractable formulation to describe the mechanical response under quasistatic loading conditions of bodies made of a large class of viscoelastic materials of arbitrary compressibility. This is achieved by describing the viscoelasticity of the material within a two-potential mixed Lagrangian formulation, wherein the deformation field, a pressure field that ensues from a suitably defined Legendre transform, and an internal variable of state  $\mathbf{F}^v$  that describes the viscous part of the deformation are the independent fields. Consistent with the prevailing view that viscous dissipation in soft organic materials is primarily due to the friction between the underlying long molecular chains and that this process is inherently isochoric, the internal variable  $\mathbf{F}^v$  is required to satisfy the constraint  $\det \mathbf{F}^v = 1$ . The second objective of this paper is to put forth a robust numerical method of solution for the resulting initial–boundary-value problem. There are two main challenges in doing so that amount to choosing appropriate space and time discretizations that lead to a stable and hence convergent formulation. To address these challenges, we make use of a finite-element (FE) discretization of space based on the Variational Multiscale (VMS) method and of a finite-difference (FD) discretization of time together with a new time integration scheme that preserves the constraint  $\det \mathbf{F}^v = 1$  identically.

The paper is organized as follows. We begin in Section 2 by formulating the general initial–boundary-value problem for the class of viscoelastic materials of interest in this work. We then present the associated numerical method of solution in Section 3. Aimed at showcasing the capabilities of the proposed method, we work out numerical solutions for a series of test cases in Section 4. We close by summarizing the main findings of this work in Section 5.

## 2. Formulation of the initial–boundary-value problem in finite viscoelasticity

### 2.1. Initial configuration and kinematics

Consider a body that in its initial configuration, at time  $t = 0$ , occupies the open domain  $\Omega_0 \subset \mathbb{R}^3$ , with boundary  $\partial\Omega_0$  and outward unit normal  $\mathbf{N}$ . We identify material points by their initial position vector  $\mathbf{X} \in \Omega_0$ . At a later time  $t \in (0, T]$ , in response to boundary conditions and body forces to be described below, the position vector  $\mathbf{X}$  of a material point may occupy a new position  $\mathbf{x}$  specified by an invertible mapping  $\varphi$  from  $\Omega_0$  to the current configuration  $\Omega(t) \subset \mathbb{R}^3$ . We write

$$\mathbf{x} = \varphi(\mathbf{X}, t)$$

and the associated deformation gradient and Lagrangian velocity fields at  $\mathbf{X} \in \Omega_0$  and  $t \in (0, T]$  as

$$\mathbf{F}(\mathbf{X}, t) = \nabla \varphi(\mathbf{X}, t) = \frac{\partial \varphi}{\partial \mathbf{X}}(\mathbf{X}, t) \quad \text{and} \quad \mathbf{V}(\mathbf{X}, t) = \dot{\varphi}(\mathbf{X}, t) = \frac{\partial \varphi}{\partial t}(\mathbf{X}, t).$$

Throughout, we shall use the “dot” notation to denote the material time derivative (i.e., with  $\mathbf{X}$  held fixed) of field quantities.

### 2.2. Constitutive behavior

The focus of this work is on soft organic materials that are isotropic and of elastomeric type. Accordingly, making use of the two-potential formalism (Halphen and Nguyen, 1975; Ziegler and Wehrli, 1987; Kumar and Lopez-Pamies, 2016), the constitutive behavior of the body is taken to be characterized by two thermodynamic potentials, a free energy of the general form

$$\psi(\mathbf{F}, \mathbf{F}^v) = \psi^{\text{Eq}}(\mathbf{F}) + \psi^{\text{NEq}}(\mathbf{F}\mathbf{F}^{v-1}) \quad (1)$$

that describes how the material stores energy through elastic deformation and a dissipation potential of the general form

$$\phi(\mathbf{F}, \mathbf{F}^v, \dot{\mathbf{F}}^v) = \begin{cases} \frac{1}{2} \dot{\mathbf{F}}^v \mathbf{F}^{v-1} \cdot [2 \eta_{\mathcal{K}}(\mathbf{F}, \mathbf{F}^v) \mathcal{K} \dot{\mathbf{F}}^v \mathbf{F}^{v-1}] & \text{if } \text{tr}(\dot{\mathbf{F}}^v \mathbf{F}^{v-1}) = 0 \\ +\infty & \text{otherwise} \end{cases} \quad (2)$$

that describes how the material dissipates energy through viscous deformation. In these expressions, the second-order tensor  $\mathbf{F}^v$  is an internal variable of state that roughly stands for the “viscous part” of the deformation gradient  $\mathbf{F}$ ,  $\psi^{\text{Eq}}(\mathbf{F})$  is a non-negative

function that characterizes the elastic energy storage in the material at states of thermodynamic equilibrium, the non-negative function  $\psi^{\text{NEq}}(\mathbf{F}, \mathbf{F}^v)$  characterizes the additional elastic energy storage at non-equilibrium states (i.e., the part of the energy that gets dissipated eventually),  $\mathcal{K}_{ijkl} = \frac{1}{2} \left( \delta_{ik}\delta_{jl} + \delta_{il}\delta_{jk} - \frac{2}{3}\delta_{ij}\delta_{kl} \right)$  denotes the standard deviatoric orthogonal projection tensor, and the function  $\eta_{\mathcal{K}}(\mathbf{F}, \mathbf{F}^v) \geq 0$  characterizes the (deviatoric) viscosity of the material. Material frame indifference and material isotropy require that  $\psi^{\text{Eq}}(\mathbf{Q}\mathbf{F}\mathbf{K}) = \psi^{\text{Eq}}(\mathbf{F})$ ,  $\psi^{\text{NEq}}(\mathbf{Q}\mathbf{F}\mathbf{F}^{v-1}) = \psi^{\text{NEq}}(\mathbf{F}\mathbf{F}^{v-1})$ , and  $\eta_{\mathcal{K}}(\mathbf{Q}\mathbf{F}\mathbf{K}, \mathbf{F}^v\mathbf{K}) = \eta_{\mathcal{K}}(\mathbf{F}, \mathbf{F}^v)$  for all  $\mathbf{Q}, \mathbf{K} \in \text{SO}(3)$  and arbitrary  $\mathbf{F}$  and  $\mathbf{F}^v$ . The fact that  $\eta_{\mathcal{K}}(\mathbf{F}, \mathbf{F}^v) \geq 0$  implies that the second law of thermodynamics is satisfied automatically (Kumar and Lopez-Pamies, 2016).

In this work, for definiteness, with slight abuse of notation, we concern ourselves with functions of the specific form

$$\psi^{\text{Eq}}(\mathbf{F}) = \psi^{\text{Eq}}(I_1, J), \quad \psi^{\text{NEq}}(\mathbf{F}\mathbf{F}^{v-1}) = \psi^{\text{NEq}}(I_1^e, J), \quad \eta_{\mathcal{K}}(\mathbf{F}, \mathbf{F}^v) = \eta(I_1^e, I_2^e, I_1^v), \tag{3}$$

where

$$I_1 = \text{tr } \mathbf{C}, \quad J = \sqrt{\det \mathbf{C}}, \quad I_1^v = \text{tr } \mathbf{C}^v, \quad I_1^e = \text{tr} \left( \mathbf{C}\mathbf{C}^{v-1} \right), \quad I_2^e = \frac{1}{2} \left[ \left( \mathbf{C} \cdot \mathbf{C}^{v-1} \right)^2 - \mathbf{C}^{v-1} \mathbf{C} \cdot \mathbf{C}\mathbf{C}^{v-1} \right]$$

with  $\mathbf{C} = \mathbf{F}^T\mathbf{F}$  and  $\mathbf{C}^v = \mathbf{F}^{vT}\mathbf{F}^v$ . It is a simple matter to verify that these representations satisfy the constraints imposed by material frame indifference and material isotropy. They are also sufficiently general to include as special cases a wide range of popular models for compressible and incompressible non-Gaussian elasticity (Arruda and Boyce, 1993; Beatty, 2003; Gent, 1996; Lopez-Pamies, 2010), as well as for shear-thinning and shear-thickening viscosities (Krieger, 1972; Stickel and Powell, 2005).

Granted the two thermodynamic potentials (1) and (2), it follows that the first Piola–Kirchhoff stress tensor  $\mathbf{P}$  at any material point  $\mathbf{X} \in \Omega_0$  and time  $t \in [0, T]$  is expediently given by the relation (Kumar and Lopez-Pamies, 2016)

$$\mathbf{P}(\mathbf{X}, t) = \frac{\partial \psi}{\partial \mathbf{F}}(\mathbf{F}, \mathbf{F}^v), \tag{4}$$

where  $\mathbf{F}^v$  is implicitly defined by the evolution equation

$$\begin{cases} \frac{\partial \psi}{\partial \mathbf{F}^v}(\mathbf{F}, \mathbf{F}^v) + \frac{\partial \phi}{\partial \dot{\mathbf{F}}^v}(\mathbf{F}, \mathbf{F}^v, \dot{\mathbf{F}}^v) = \mathbf{0} \\ \mathbf{F}^v(\mathbf{X}, 0) = \mathbf{I} \end{cases} \tag{5}$$

Making explicit use of the representations (3), the constitutive relation (4)–(5) specializes to

$$\mathbf{P}(\mathbf{X}, t) = 2\psi_{I_1}^{\text{Eq}}\mathbf{F} + 2\psi_{I_1^e}^{\text{NEq}}\mathbf{F}\mathbf{C}^{v-1} + \left( \psi_J^{\text{Eq}} + \psi_J^{\text{NEq}} \right) J\mathbf{F}^{-T}, \tag{6}$$

where  $\mathbf{C}^v$  is defined implicitly as the solution of the evolution equation

$$\begin{cases} \dot{\mathbf{C}}^v(\mathbf{X}, t) = \frac{2\psi_{I_1^e}^{\text{NEq}}}{\eta(I_1^e, I_2^e, I_1^v)} \left[ \mathbf{C} - \frac{1}{3} (\mathbf{C} \cdot \mathbf{C}^{v-1}) \mathbf{C}^v \right] \\ \mathbf{C}^v(\mathbf{X}, 0) = \mathbf{I} \end{cases} \tag{7}$$

and where we have made use of the notation  $\psi_{I_1}^{\text{Eq}} = \partial\psi^{\text{Eq}}(I_1, J)/\partial I_1$ ,  $\psi_J^{\text{Eq}} = \partial\psi^{\text{Eq}}(I_1, J)/\partial J$ ,  $\psi_{I_1^e}^{\text{NEq}} = \partial\psi^{\text{NEq}}(I_1^e, J)/\partial I_1^e$ ,  $\psi_J^{\text{NEq}} = \partial\psi^{\text{NEq}}(I_1^e, J)/\partial J$ . Here, it is important to note that the dependence on the internal variable  $\mathbf{F}^v$  ends up entering (6) and (7) only through the symmetric combination  $\mathbf{C}^v = \mathbf{F}^{vT}\mathbf{F}^v$ .

**Remark 1.** The interested reader is referred to Kumar and Lopez-Pamies (2016) for a complete account of the two-potential framework. Here, we remark that the constitutive relation (6)–(7) can be thought of as a generalization of the classical Zener or standard solid model (Zener, 1948) to the setting of finite deformations, one where the definition of the internal variable  $\mathbf{F}^v$  follows the standard multiplicative choice introduced in Sidoroff (1974) for finite viscoelasticity; Fig. 1 illustrates its rheological representation. Indeed, in the limit of small deformations as  $\mathbf{F} \rightarrow \mathbf{I}$ , it is straightforward to show that the constitutive relation (6)–(7) reduces to the linear viscoelastic Zener model

$$\mathbf{P}(\mathbf{X}, t) = 2\mu \boldsymbol{\varepsilon} + \Lambda \text{tr}(\boldsymbol{\varepsilon})\mathbf{I} + 2\nu(\boldsymbol{\varepsilon} - \boldsymbol{\varepsilon}^v) + \varpi \text{tr}(\boldsymbol{\varepsilon} - \boldsymbol{\varepsilon}^v)\mathbf{I} + O(\|\mathbf{F} - \mathbf{I}\|^3),$$

where  $\boldsymbol{\varepsilon} = 1/2(\mathbf{F} + \mathbf{F}^T - 2\mathbf{I})$  stands for the infinitesimal strain tensor and  $\boldsymbol{\varepsilon}^v = 1/2(\mathbf{F}^v + \mathbf{F}^{vT} - 2\mathbf{I})$  is solution of the evolution equation

$$\begin{cases} \dot{\boldsymbol{\varepsilon}}^v(\mathbf{X}, t) = \frac{\nu}{\eta_0} \left[ \boldsymbol{\varepsilon} - \boldsymbol{\varepsilon}^v - \frac{1}{3} \text{tr}(\boldsymbol{\varepsilon} - \boldsymbol{\varepsilon}^v)\mathbf{I} \right] \\ \boldsymbol{\varepsilon}^v(\mathbf{X}, 0) = \mathbf{0} \end{cases}$$

In these expressions,  $\mu = 2\partial\psi^{\text{Eq}}(3, 1)/\partial I_1 = -\partial\psi^{\text{Eq}}(3, 1)/\partial J$  and  $\Lambda = \partial^2\psi^{\text{Eq}}(3, 1)/\partial J^2 + 4\partial^2\psi^{\text{Eq}}(3, 1)/\partial I_1^2 + 4\partial^2\psi^{\text{Eq}}(3, 1)/\partial I_1\partial J - \mu$  stand for the initial shear modulus and first Lamé constant associated with the elastic energy in equilibrium, similarly,  $\nu = 2\partial\psi^{\text{NEq}}(3, 1)/\partial I_1^e = -\partial\psi^{\text{NEq}}(3, 1)/\partial J$  and  $\varpi = \partial^2\psi^{\text{NEq}}(3, 1)/\partial J^2 + 4\partial^2\psi^{\text{NEq}}(3, 1)/\partial I_1^{e2} + 4\partial^2\psi^{\text{NEq}}(3, 1)/\partial I_1^e\partial J - \nu$  stand for the initial shear modulus and first Lamé constant associated with the non-equilibrium elastic energy, while  $\eta_0 = \eta(3, 3, 3)$ . In addition, the constitutive relation (6)–(7) includes two fundamental models as limiting cases. The first one, which corresponds to setting the viscosity function either to  $\eta = 0$  or  $\eta = +\infty$ , is that of a *non-Gaussian elastic solid*. The second one, which corresponds to setting the equilibrium and non-equilibrium energies to  $\psi^{\text{Eq}} = 0$  and  $\psi^{\text{NEq}} = +\infty$ , is that of an *incompressible non-Newtonian fluid*.

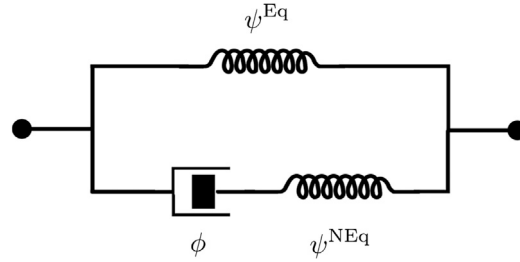


Fig. 1. Rheological representation of the two-potential model (6)–(7) for viscoelasticity.

2.3. Boundary conditions and body forces

The external stimuli applied to the body comprise both prescribed mechanical boundary data and body forces in the bulk. Precisely, on a portion  $\partial\Omega_0^D$  of the boundary  $\partial\Omega_0$  the deformation field  $\varphi(\mathbf{X}, t)$  is taken to be given by a known function  $\bar{\varphi}(\mathbf{X}, t)$ , while the complementary part of the boundary  $\partial\Omega_0^N = \partial\Omega_0 \setminus \partial\Omega_0^D$  is subjected to a prescribed nominal traction  $\bar{\mathbf{t}}(\mathbf{X}, t)$ . That is,

$$\begin{cases} \varphi(\mathbf{X}, t) = \bar{\varphi}(\mathbf{X}, t), & (\mathbf{X}, t) \in \partial\Omega_0^D \times [0, T] \\ \mathbf{P}(\mathbf{X}, t)\mathbf{N} = \bar{\mathbf{t}}(\mathbf{X}, t), & (\mathbf{X}, t) \in \partial\Omega_0^N \times [0, T] \end{cases} \quad (8)$$

Throughout  $\Omega_0$ , we also consider that the body is subjected to a mechanical body force with density

$$\mathbf{B}(\mathbf{X}, t), \quad (\mathbf{X}, t) \in \Omega_0 \times [0, T]. \quad (9)$$

2.4. Governing equations: The pure-displacement formulation

Absent inertia, the relevant equations of balance of linear and angular momenta read simply as  $\text{Div } \mathbf{P} + \mathbf{B} = \mathbf{0}$  and  $\mathbf{P}\mathbf{F}^T = \mathbf{F}\mathbf{P}^T$  for  $(\mathbf{X}, t) \in \Omega_0 \times [0, T]$ . The latter is automatically satisfied by virtue of the objectivity of the functions (3) and so the governing equations for the response of the body reduce to the following initial–boundary-value problem:

$$\begin{cases} \text{Div} \left[ 2\psi_{I_1}^{\text{Eq}} \nabla \varphi + 2\psi_{I_1^e}^{\text{NEq}} \nabla \varphi \mathbf{C}^{v-1} + (\psi_J^{\text{Eq}} + \psi_J^{\text{NEq}}) J \nabla \varphi^{-T} \right] + \mathbf{B} = \mathbf{0}, & (\mathbf{X}, t) \in \Omega_0 \times [0, T] \\ \varphi(\mathbf{X}, t) = \bar{\varphi}(\mathbf{X}, t), & (\mathbf{X}, t) \in \partial\Omega_0^D \times [0, T] \\ \left[ 2\psi_{I_1}^{\text{Eq}} \nabla \varphi + 2\psi_{I_1^e}^{\text{NEq}} \nabla \varphi \mathbf{C}^{v-1} + (\psi_J^{\text{Eq}} + \psi_J^{\text{NEq}}) J \nabla \varphi^{-T} \right] \mathbf{N} = \bar{\mathbf{t}}(\mathbf{X}, t), & (\mathbf{X}, t) \in \partial\Omega_0^N \times [0, T] \\ \varphi(\mathbf{X}, 0) = \mathbf{X}, & \mathbf{X} \in \Omega_0 \end{cases} \quad (10)$$

coupled with the evolution equation

$$\begin{cases} \dot{\mathbf{C}}^v(\mathbf{X}, t) = \frac{2\psi_{I_1^e}^{\text{NEq}}}{\eta(I_1^e, I_2^e, I_1^v)} \left[ \nabla \varphi^T \nabla \varphi - \frac{1}{3} (\nabla \varphi^T \nabla \varphi \cdot \mathbf{C}^{v-1}) \mathbf{C}^v \right], & (\mathbf{X}, t) \in \Omega_0 \times [0, T] \\ \mathbf{C}^v(\mathbf{X}, 0) = \mathbf{I}, & \mathbf{X} \in \Omega_0 \end{cases} \quad (11)$$

for the deformation field  $\varphi(\mathbf{X}, t)$  and the internal variable  $\mathbf{C}^v(\mathbf{X}, t)$ . Note that we have tacitly assumed that the body is free of stresses in its initial configuration.

2.5. Governing equations: A mixed deformation-pressure formulation

As announced in the Introduction, one of the objectives of this work is to put forth a unified formulation to describe the mechanical response of viscoelastic bodies of arbitrary compressibility. In order to deal with highly compressible as well as with nearly or fully incompressible materials, it is convenient to deal *not* with Eqs. (10)–(11) directly, but with an alternative set of equations wherein a pressure field (and not just the deformation field) is also an unknown. Much like in the simpler setting of elasticity, as outlined next, the derivation of such a mixed set of equations hinges on the introduction on an appropriate Legendre transform.

Consider the following function

$$\psi(I_1, I_1^e, J) = \psi^{\text{Eq}}(I_1, J) + \psi^{\text{NEq}}(I_1^e, J)$$

alongside its partial Legendre transform

$$\psi^*(I_1, I_1^e, p) = \max \{ p(J - 1) - \psi(I_1, I_1^e, J) \}. \quad (12)$$

For the physically relevant case when  $\psi(I_1, I_1^e, J)$  is convex in its third argument, it follows that

$$\psi(I_1, I_1^e, J) = (\psi^*)^*(I_1, I_1^e, J) = \max_p \{p(J - 1) - \psi^*(I_1, I_1^e, p)\}.$$

In turn, it follows that the first Piola–Kirchhoff stress tensor (4) can be rewritten in terms of the dual function (12) as

$$\mathbf{P}(\mathbf{X}, t) = \frac{\partial \psi}{\partial \mathbf{F}}(I_1, I_1^e, J) = -\frac{\partial \psi^*}{\partial \mathbf{F}}(I_1, I_1^e, p) + pJ\mathbf{F}^{-T} \quad \text{with} \quad J = 1 + \frac{\partial \psi^*}{\partial p}(I_1, I_1^e, p), \quad (13)$$

which leads to the alternative mixed set of governing equations

$$\left\{ \begin{array}{l} \text{Div} \left[ -\frac{\partial \psi^*}{\partial \mathbf{F}}(I_1, I_1^e, p) + pJ\nabla \boldsymbol{\varphi}^{-T} \right] + \mathbf{B} = \mathbf{0}, \quad (\mathbf{X}, t) \in \Omega_0 \times [0, T] \\ J - 1 - \frac{\partial \psi^*}{\partial p}(I_1, I_1^e, p) = 0, \quad (\mathbf{X}, t) \in \Omega_0 \times [0, T] \\ \boldsymbol{\varphi}(\mathbf{X}, t) = \bar{\boldsymbol{\varphi}}(\mathbf{X}, t), \quad (\mathbf{X}, t) \in \partial\Omega_0^D \times [0, T] \\ \left[ -\frac{\partial \psi^*}{\partial \mathbf{F}}(I_1, I_1^e, p) + pJ\nabla \boldsymbol{\varphi}^{-T} \right] \mathbf{N} = \bar{\mathbf{t}}(\mathbf{X}, t), \quad (\mathbf{X}, t) \in \partial\Omega_0^N \times [0, T] \\ \boldsymbol{\varphi}(\mathbf{X}, 0) = \mathbf{X}, \quad \mathbf{X} \in \Omega_0 \end{array} \right. \quad (14)$$

and

$$\left\{ \begin{array}{l} \mathbf{C}^v(\mathbf{X}, t) = \frac{2\psi_{I_1^e}^{\text{NEq}}}{\eta(I_1^e, I_2^e, I_1^v)} \left[ \nabla \boldsymbol{\varphi}^T \nabla \boldsymbol{\varphi} - \frac{1}{3} (\nabla \boldsymbol{\varphi}^T \nabla \boldsymbol{\varphi} \cdot \mathbf{C}^{v-1}) \mathbf{C}^v \right], \quad (\mathbf{X}, t) \in \Omega_0 \times [0, T] \\ \mathbf{C}^v(\mathbf{X}, 0) = \mathbf{I}, \quad \mathbf{X} \in \Omega_0 \end{array} \right. \quad (15)$$

for the deformation field  $\boldsymbol{\varphi}(\mathbf{X}, t)$ , the pressure field  $p(\mathbf{X}, t)$ , and the internal variable  $\mathbf{C}^v(\mathbf{X}, t)$ .

In the remaining of this work, to make the presentation and discussion precise, we shall use equilibrium and non-equilibrium free-energy functions of the particular form

$$\psi^{\text{Eq}}(I_1, J) = \Psi^{\text{Eq}}(I_1) - \mu \ln J + \frac{\kappa}{2}(J - 1)^2 \quad \text{and} \quad \psi^{\text{NEq}}(I_1, J) = \Psi^{\text{NEq}}(I_1^e) - \nu \ln J + \frac{\kappa}{2}(J - 1)^2 \quad (16)$$

as a template. Here, we recall that  $\mu$  and  $\nu$  denote the initial shear moduli associated with the equilibrium and non-equilibrium elastic energies of the material at hand, while  $\kappa \geq 0$  is a parameter that describes its compressibility in a monotonic fashion, precisely, the larger the value of  $\kappa$  the smaller the compressibility of the material. For the class of functions (16), the partial Legendre transform (12) reads

$$\psi^*(I_1, I_1^e, p) = -\Psi^{\text{Eq}}(I_1) - \Psi^{\text{NEq}}(I_1^e) + \frac{p^2 - 4\kappa(\kappa + \mu + \nu) - 4\kappa p}{8\kappa} + \frac{(2\kappa + p)\sqrt{8\kappa(\mu + \nu) + (2\kappa + p)^2}}{8\kappa} \\ + (\mu + \nu) \ln \left[ \frac{\sqrt{8\kappa(\mu + \nu) + (2\kappa + p)^2} + 2\kappa + p}{4\kappa} \right]$$

and the governing equations (14)–(15) specialize to

$$\left\{ \begin{array}{l} \text{Div} \left[ 2\frac{\partial \Psi^{\text{Eq}}}{\partial I_1}(I_1)\nabla \boldsymbol{\varphi} + 2\frac{\partial \Psi^{\text{NEq}}}{\partial I_1^e}(I_1^e)\nabla \boldsymbol{\varphi} \mathbf{C}^{v-1} + pJ\nabla \boldsymbol{\varphi}^{-T} \right] + \mathbf{B} = \mathbf{0}, \quad (\mathbf{X}, t) \in \Omega_0 \times [0, T] \\ J - 1 - \frac{p - 2\kappa + \sqrt{8\kappa(\mu + \nu) + (2\kappa + p)^2}}{4\kappa} = 0, \quad (\mathbf{X}, t) \in \Omega_0 \times [0, T] \\ \boldsymbol{\varphi}(\mathbf{X}, t) = \bar{\boldsymbol{\varphi}}(\mathbf{X}, t), \quad (\mathbf{X}, t) \in \partial\Omega_0^D \times [0, T] \\ \left[ 2\frac{\partial \Psi^{\text{Eq}}}{\partial I_1}(I_1)\nabla \boldsymbol{\varphi} + 2\frac{\partial \Psi^{\text{NEq}}}{\partial I_1^e}(I_1^e)\nabla \boldsymbol{\varphi} \mathbf{C}^{v-1} + pJ\nabla \boldsymbol{\varphi}^{-T} \right] \mathbf{N} = \bar{\mathbf{t}}(\mathbf{X}, t), \quad (\mathbf{X}, t) \in \partial\Omega_0^N \times [0, T] \\ \boldsymbol{\varphi}(\mathbf{X}, 0) = \mathbf{X}, \quad \mathbf{X} \in \Omega_0 \end{array} \right. \quad (17)$$

and

$$\left\{ \begin{array}{l} \mathbf{C}^v(\mathbf{X}, t) = \frac{2\frac{\partial \Psi^{\text{NEq}}}{\partial I_1^e}(I_1^e)}{\eta(I_1^e, I_2^e, I_1^v)} \left[ \nabla \boldsymbol{\varphi}^T \nabla \boldsymbol{\varphi} - \frac{1}{3} (\nabla \boldsymbol{\varphi}^T \nabla \boldsymbol{\varphi} \cdot \mathbf{C}^{v-1}) \mathbf{C}^v \right], \quad (\mathbf{X}, t) \in \Omega_0 \times [0, T] \\ \mathbf{C}^v(\mathbf{X}, 0) = \mathbf{I}, \quad \mathbf{X} \in \Omega_0 \end{array} \right. \quad (18)$$

again, for the deformation field  $\boldsymbol{\varphi}(\mathbf{X}, t)$ , the pressure field  $p(\mathbf{X}, t)$ , and the internal variable  $\mathbf{C}^v(\mathbf{X}, t)$ .

In general, the nonlinear initial–boundary–value problem (17)–(18), much like its more general version (14)–(15), can only be solved numerically. As pointed out in the Introduction, the construction of such numerical solutions is challenging on two counts. The fact that the internal variable  $\mathbf{C}^v$  defined by system of ordinary differential Eqs. (18) satisfies the nonconvex constraint  $\det \mathbf{C}^v = 1$

poses one of the main difficulties. Indeed, as is well-known from the related literature on finite plasticity (Simo, 1992), commonly used time integration schemes are unable to deliver solutions that satisfy the constraint  $\det \mathbf{C}^v = 1$ . The other main difficulty is posed by the geometric nonlinearity associated with finite deformations and the transition from very compressible to incompressible material behavior when  $\kappa$  is increased from  $\kappa = 0$  to  $\kappa = +\infty$ .

### 3. The proposed numerical method

In this section, we introduce a numerical scheme to solve the initial–boundary-value problem (17)–(18) that is capable of robustly handling the above-outlined challenges. The idea is twofold. On the one hand, we make use of a FE discretization of space based on the VMS method. On the other hand, we make use of a FD discretization of time in conjunction with a time integration scheme that preserves the constraint  $\det \mathbf{F}^v = 1$  identically. We begin in Section 3.1 by spelling out the weak form of the governing equations (17)–(18). In Section 3.2, we further rewrite the PDE part of the weak form into a stabilized weak form. In Sections 3.3 and 3.4, we layout the time and space discretizations. Finally, in Section 3.5, we present the method for the solution of the resulting discretized equations and detail, in Sections 3.6 and 3.7, the new determinant-preserving time integration scheme.

#### 3.1. Weak form of the governing equations

A standard calculation shows that the weak form of the initial–boundary-value problem (17)–(18) specializes to finding  $\varphi(\mathbf{X}, t) \in \mathcal{Y}$  and  $p(\mathbf{X}, t) \in \mathcal{P}$  such that

$$\left\{ \begin{aligned} \int_{\Omega_0} \nabla \eta \cdot \left[ 2 \frac{\partial \Psi^{\text{Eq}}}{\partial I_1} (I_1) \nabla \varphi + 2 \frac{\partial \Psi^{\text{NEq}}}{\partial I_1^e} (I_1^e) \nabla \varphi \mathbf{C}^{v-1} + p J \nabla \varphi^{-T} \right] d\mathbf{X} \\ = \int_{\Omega_0} \eta \cdot \mathbf{B} d\mathbf{X} + \int_{\partial \Omega_0^N} \eta \cdot \bar{\mathbf{t}} d\mathbf{X} \quad \forall \eta \in \mathcal{Y}_0, t \in [0, T] \\ \int_{\Omega_0} q \left[ J - 1 - \frac{p - 2\kappa + \sqrt{8\kappa(\mu + \nu) + (2\kappa + p)^2}}{4\kappa} \right] d\mathbf{X} = 0 \quad \forall q \in \mathcal{P}, t \in [0, T] \end{aligned} \right. \quad (19)$$

with  $\mathbf{C}^v(\mathbf{X}, t)$  defined by

$$\left\{ \begin{aligned} \dot{\mathbf{C}}^v(\mathbf{X}, t) &= \mathbf{G}(\nabla \varphi(\mathbf{X}, t), \mathbf{C}^v(\mathbf{X}, t)) \\ &\equiv \frac{2 \frac{\partial \Psi^{\text{NEq}}}{\partial I_1^e} (I_1^e)}{\eta(I_1^e, I_2^e, I_1^v)} \left[ \nabla \varphi^T \nabla \varphi - \frac{1}{3} (\nabla \varphi^T \nabla \varphi \cdot \mathbf{C}^{v-1}) \mathbf{C}^v \right], \quad (\mathbf{X}, t) \in \Omega_0 \times [0, T] \\ \mathbf{C}^v(\mathbf{X}, 0) &= \mathbf{I}, \quad \mathbf{X} \in \Omega_0 \end{aligned} \right. \quad (20)$$

where  $\mathcal{Y}$  and  $\mathcal{P}$  are sufficiently large sets of admissible deformation  $\varphi$  and pressure  $p$  fields. Similarly,  $\mathcal{Y}_0$  stands for a sufficiently large set of test functions  $\eta$ . Formally,

$$\mathcal{Y} = \{ \varphi : \varphi(\mathbf{X}, t) = \bar{\varphi}(\mathbf{X}, t), \mathbf{X} \in \partial \Omega_0^D \} \quad \text{and} \quad \mathcal{Y}_0 = \{ \eta : \eta(\mathbf{X}, t) = \mathbf{0}, \mathbf{X} \in \partial \Omega_0^D \}.$$

Moreover, for later convenience, we have introduced the function  $\mathbf{G}$  to denote the right-hand side of the evolution equation for  $\mathbf{C}^v$ .

#### 3.2. A stabilized weak form via the variational multiscale method

Following in the footsteps of Masud and Truster (2013), we proceed by recasting the PDE part (19) of the governing equations in a stabilized form derived by the VMS method, which will allow us to choose any arbitrary combination of approximations for the deformation and pressure fields in the FE discretization of space proposed below.

The starting point in the construction of a stabilized form of (19) is to consider the split of the deformation field

$$\varphi(\mathbf{X}, t) = \tilde{\varphi} \circ \hat{\varphi}$$

into a coarse-scale contribution  $\hat{\varphi}$  and a fine-scale contribution  $\tilde{\varphi}$ ; in this last expression, the symbol “ $\circ$ ” stands for the composition operator. When viewed within the context of a numerical method of solution, the coarse-scale mapping  $\hat{\varphi}$  stands for the part of the deformation field  $\varphi(\mathbf{X}, t)$  that can be represented by the basis functions used in the numerical approximation. On the other hand, the fine-scale mapping  $\tilde{\varphi}$  stands for the remaining unrepresented part. We write the corresponding coarse-scale and fine-scale displacement fields as  $\hat{\mathbf{u}}$  and  $\tilde{\mathbf{u}}$ , and note that

$$\mathbf{F}(\mathbf{X}, t) = \frac{\partial \varphi}{\partial \mathbf{X}} = \frac{\partial \tilde{\varphi}}{\partial \zeta} \frac{\partial \hat{\varphi}}{\partial \mathbf{X}} = \tilde{\mathbf{F}} \hat{\mathbf{F}}, \quad \zeta = \hat{\varphi}(\mathbf{X}, t),$$

where  $\hat{\mathbf{F}}$  and  $\tilde{\mathbf{F}}$  are the coarse-scale and fine-scale deformation gradients.

Next, making use of the analogous split of the weighting function

$$\eta(\mathbf{X}, t) = \underbrace{\tilde{\varphi} \circ \hat{\eta}}_{\hat{\eta}_{\tilde{\varphi}}} + \underbrace{\tilde{\eta} \circ \hat{\varphi}}_{\tilde{\eta}_{\hat{\varphi}}}$$

into a coarse-scale part  $\hat{\eta}$  and a fine-scale part  $\tilde{\eta}$ , as well as of the notation

$$\mathbf{S}(\mathbf{X}, t) = \mathbf{F}^{-1} \mathbf{P} = \mathbf{F}^{-1} \left[ 2 \frac{\partial \Psi^{\text{Eq}}}{\partial I_1} (I_1) \nabla \boldsymbol{\varphi} + 2 \frac{\partial \Psi^{\text{NEq}}}{\partial I_1^e} (I_1^e) \nabla \boldsymbol{\varphi} \mathbf{C}^{v-1} + p J \nabla \boldsymbol{\varphi}^{-T} \right]$$

for the second Piola–Kirchhoff stress tensor, the residuals of the PDE part (19) of the governing equations can be split into the following two residuals:

*Coarse-scale residual*

$$\left\{ \begin{aligned} \hat{R}_u(\hat{\eta}; \hat{\mathbf{u}}, \hat{\mathbf{u}}, p, \mathbf{C}^v) &\equiv \int_{\Omega_0} \tilde{\mathbf{F}} \nabla \hat{\eta} \cdot \mathbf{F} \mathbf{S} \, d\mathbf{X} - \int_{\Omega_0} \hat{\eta}_{\tilde{\varphi}} \cdot \mathbf{B} \, d\mathbf{X} - \int_{\partial \Omega_0^N} \hat{\eta}_{\tilde{\varphi}} \cdot \bar{\mathbf{t}} \, d\mathbf{X} \\ \hat{R}_p(q; \hat{\mathbf{u}}, \hat{\mathbf{u}}, p, \mathbf{C}^v) &\equiv \int_{\Omega_0} q \left[ J - 1 - \frac{p - 2\kappa + \sqrt{8\kappa(\mu + \nu) + (2\kappa + p)^2}}{4\kappa} \right] d\mathbf{X} \end{aligned} \right. \quad (21)$$

*Fine-scale residual*

$$\tilde{R}_u(\tilde{\eta}; \hat{\mathbf{u}}, \tilde{\mathbf{u}}, p, \mathbf{C}^v) \equiv \int_{\Omega_0} \nabla \tilde{\eta} \cdot \mathbf{F} \mathbf{S} \, d\mathbf{X} - \int_{\Omega_0} \tilde{\eta}_{\hat{\varphi}} \cdot \mathbf{B} \, d\mathbf{X} - \int_{\partial \Omega_0^N} \tilde{\eta}_{\hat{\varphi}} \cdot \bar{\mathbf{t}} \, d\mathbf{X}$$

At this stage, we need to make a constitutive choice for the modeling of the fine-scale problem. Consistent with the eventual use of a Newton–Raphson scheme to solve the nonlinear algebraic equations that result from the FE space discretization of the coarse-scale problem, we make use of the standard choice based on the linearization of the fine scales around the current solution of the coarse scale, that is, around  $\tilde{\mathbf{u}} = \mathbf{0}$ . Precisely, we make use of the constitutive choice introduced in Masud and Truster (2013), which is based on bubble functions that vanish at the boundary of their support. Following then the same steps presented in Section 2.3 and 3 in Masud and Truster (2013) allows to reduce the coarse-scale residual (21) to its final form

$$\left\{ \begin{aligned} R_u(\eta; \mathbf{u}, p, \mathbf{C}^v) &\equiv \int_{\Omega_0} \mathbf{S} \cdot \delta \mathbf{E}(\eta) \, d\mathbf{X} - \int_{\Omega_0} \eta \cdot \mathbf{B} \, d\mathbf{X} - \int_{\partial \Omega_0^N} \eta \cdot \bar{\mathbf{t}} \, d\mathbf{X} \\ &\quad - \int_{\Omega_0} (\text{Div} [\nabla \eta \mathbf{S} + \nabla \boldsymbol{\varphi} (\mathbf{C} \delta \mathbf{E}(\eta))]) \cdot \boldsymbol{\tau} \hat{\mathbf{R}} \, d\mathbf{X} = 0 \\ R_p(q; \mathbf{u}, p, \mathbf{C}^v) &\equiv \int_{\Omega_0} q \left[ J - 1 - \frac{p - 2\kappa + \sqrt{8\kappa(\mu + \nu) + (2\kappa + p)^2}}{4\kappa} \right] d\mathbf{X} \\ &\quad - \int_{\Omega_0} (\text{Div} [q(\nabla \boldsymbol{\varphi} \mathbf{S} - p J \nabla \boldsymbol{\varphi}^{-T})]) \cdot \boldsymbol{\tau} \hat{\mathbf{R}} \, d\mathbf{X} = 0 \end{aligned} \right.$$

In these expressions, we have reverted to the notation without “hats” for simplicity,  $\delta \mathbf{E}(\eta) = 1/2(\nabla \boldsymbol{\varphi}^T \nabla \eta + \nabla \eta^T \nabla \boldsymbol{\varphi})$ ,  $\mathbf{C} = 4\partial^2 \psi / \partial \mathbf{C} \partial \mathbf{C}$ ,

$$\boldsymbol{\tau}(\mathbf{X}, t) = \left( b \int_{\Omega_0} b \, d\mathbf{X} \right) \mathbf{T}^{-1}$$

with

$$T_{ij} = \int_{\Omega_0} \frac{\partial b}{\partial X_k} S_{kp} \frac{\partial b}{\partial X_p} \delta_{ij} \, d\mathbf{X} + \int_{\Omega_0} \frac{1}{4} \left[ F_{ip} \frac{\partial b}{\partial X_q} + \frac{\partial b}{\partial X_p} F_{iq} \right] C_{pqkl} \left[ F_{jk} \frac{\partial b}{\partial X_l} + \frac{\partial b}{\partial X_k} F_{jl} \right] d\mathbf{X},$$

$\hat{\mathbf{R}}(\mathbf{X}, t) = \text{Div} [\nabla \boldsymbol{\varphi} \mathbf{S}] + \mathbf{B}$ , where  $b(\mathbf{X}, t)$  denotes the piecewise continuous bubble function of choice.

### 3.3. Time discretization

Consider now a partition of the time interval under consideration  $[0, T]$  into discrete times  $t_k \in \{0 = t_0, t_1, \dots, t_l, t_{l+1}, \dots, t_L = T\}$ . With help of the notation  $\mathbf{u}_k(\mathbf{X}) = \mathbf{u}(\mathbf{X}, t_k)$ ,  $\boldsymbol{\varphi}_k(\mathbf{X}) = \boldsymbol{\varphi}(\mathbf{X}, t_k)$ ,  $\nabla \boldsymbol{\varphi}_k(\mathbf{X}) = \nabla \boldsymbol{\varphi}(\mathbf{X}, t_k)$ ,  $p_k(\mathbf{X}) = p(\mathbf{X}, t_k)$ ,  $\mathbf{C}_k^v(\mathbf{X}) = \mathbf{C}^v(\mathbf{X}, t_k)$ ,  $\dot{\mathbf{C}}_k^v(\mathbf{X}) = \dot{\mathbf{C}}^v(\mathbf{X}, t_k)$ , the governing equations at any given discrete time  $t_k$  can be written in the compact form

$$\left\{ \begin{aligned} R_u(\eta; \mathbf{u}_k, p_k, \mathbf{C}_k^v) &= 0 \quad \forall \eta \in \mathcal{Y}_0 \\ R_p(q; \mathbf{u}_k, p_k, \mathbf{C}_k^v) &= 0 \quad \forall q \in \mathcal{P} \end{aligned} \right. \quad (22)$$

with  $\mathbf{C}_k^v(\mathbf{X})$  defined by

$$\mathbf{C}_k^v(\mathbf{X}) = \mathbf{G}(\nabla \boldsymbol{\varphi}_k(\mathbf{X}), \mathbf{C}_k^v(\mathbf{X})), \quad (23)$$

where we emphasize that we are yet to choose an explicit or implicit time discretization for  $\dot{\mathbf{C}}_k^v(\mathbf{X})$  in terms of  $\mathbf{C}^v(\mathbf{X}, t)$ .

### 3.4. Space discretization

Having discretized the stabilized governing equations (22)–(23) in time, the next step is to further discretize them in space. To that end, consider a partition of the domain  $\Omega_0$  occupied by the body in its initial configuration into non-overlapping finite elements  $\{\Omega^e\}_{e=1}^{n_{el}}$ . Given this partition, we look for approximate solutions  ${}^h\boldsymbol{\varphi}_k(\mathbf{X})$  and  ${}^h p_k(\mathbf{X})$  of the deformation field  $\boldsymbol{\varphi}_k(\mathbf{X})$  and the pressure field  $p_k(\mathbf{X})$  at time  $t_k$  in the FE space consisting of piecewise continuous polynomial functions:

$$\mathcal{Y}^h = \{\boldsymbol{\varphi} \in \mathcal{Y} : \boldsymbol{\varphi} \in \mathbf{C}^0(\Omega_0), \boldsymbol{\varphi} \in \mathcal{P}_k(\Omega^e)\} \quad \text{and} \quad \mathcal{P}^h = \{p \in \mathcal{P} : p \in \mathcal{P}_k(\Omega^e)\},$$

where  $\mathcal{P}_k(\Omega^e)$  stands for the set of complete polynomials of order  $k$  on  $\Omega^e$ . Consistent with this FE discretization of space, we choose a piecewise continuous bubble function  $b(\mathbf{X}, t)$  with compact support in each finite element  $\Omega^e$ .

It follows that Eqs. (22)–(23) reduce to a system of nonlinear algebraic equations for the resulting global degrees of freedom, say  ${}^h\boldsymbol{\varphi}_k^{(n)}$  and  ${}^h p_k^{(n)}$ , that depend on the values, say  ${}^h\mathbf{C}_k^v$ , of the internal variable  $\mathbf{C}_k^v$  at the Gaussian quadrature points employed to carry out the integrals in (22). We write this system as

$$\begin{cases} \mathcal{G}_1({}^h\boldsymbol{\varphi}_k^{(n)}, {}^h p_k^{(n)}, {}^h\mathbf{C}_k^v) = 0 \\ \mathcal{G}_2({}^h\boldsymbol{\varphi}_k^{(n)}, {}^h p_k^{(n)}, {}^h\mathbf{C}_k^v) = 0 \end{cases} \quad (24)$$

### 3.5. The solver: A Newton-like method staggered with a determinant-preserving time integration scheme

Having discretized the governing equations (19)–(20) into the system of coupled nonlinear algebraic Eqs. (24) for the global degrees of freedom  ${}^h\boldsymbol{\varphi}_k^{(n)}$ ,  ${}^h p_k^{(n)}$ , and the internal variables  ${}^h\mathbf{C}_k^v$  at the Gaussian quadrature points at time  $t_k$ , the final step is to solve these for a given domain  $\Omega_0$  of the body, given constitutive functions (3) describing the viscoelasticity of the material, and given boundary conditions and body forces (8)–(9). We do so by following a staggered scheme, which involves solving the Eqs. (24)<sub>1</sub> and (24)<sub>2</sub> iteratively one after the other at every time step  $t_k$  until convergence is reached.

For fixed  ${}^h\mathbf{C}_k^v$ , Eq. (24)<sub>1</sub> amounts to a finite elastostatics problem formulated with mixed finite elements. Therefore, to solve for  ${}^h\boldsymbol{\varphi}_k^{(n)}$ ,  ${}^h p_k^{(n)}$  at fixed  ${}^h\mathbf{C}_k^v$  we make use of a Newton-like nonlinear method.

For fixed  ${}^h\boldsymbol{\varphi}_k^{(n)}$  and  ${}^h p_k^{(n)}$ , Eq. (24)<sub>2</sub> corresponds to a nonlinear system of first-order ODEs wherein the constraint of incompressibility  $\det {}^h\mathbf{C}_k^v = 1$  is built-in. As alluded to above, it is well-known that commonly used time integration schemes, such as the popular backward Euler scheme, are unable to deliver solutions that satisfy this non-convex constraint (Simo, 1992; Kumar and Lopez-Pamies, 2016). More specifically, commonly used time integration schemes deliver determinant values such that  $|\det {}^h\mathbf{C}_k^v - 1| = \beta \Delta t_k^r$  with  $\beta \gg 1$ , where  $\Delta t_k = t_{k+1} - t_k$  and  $r$  denotes the order of accuracy of the scheme (e.g.,  $r = 1$  for the backward Euler scheme), which renders them unacceptably inaccurate. Among implicit methods, an early *ad-hoc* remedy for this shortcoming was to make use of the exponential backward Euler scheme, which satisfies the determinant constraint identically (Hochbruck and Ostermann, 2010). More recently, among explicit methods, it has been shown that certain Runge–Kutta methods of high order deliver solutions that satisfy the determinant constraint, not identically but to their high degree of accuracy such that  $|\det {}^h\mathbf{C}_k^v - 1| = \beta \Delta t_k^r$  with  $\beta \sim 1$  (Kumar and Lopez-Pamies, 2016; Lawson, 1966).

In the sequel, we propose a scheme that allows to convert any explicit or implicit time integration scheme of any order into a stable scheme that preserves the constraint  $\det {}^h\mathbf{C}_k^v = 1$  identically.

### 3.6. The proposed time integration scheme

Consider the generic system of (linear or nonlinear) first-order ODEs

$$\begin{cases} \dot{\mathbf{Y}} = \mathbf{M}(t, \mathbf{Y}), & t \in (0, T] \\ \det \mathbf{Y} = 1, & t \in [0, T] \\ \mathbf{Y}(0) = \mathbf{Y}_0 \end{cases}, \quad (25)$$

where  $\mathbf{Y} \in \mathbb{R}^{N \times N}$ ,  $N \in \mathbb{N}$ . Making use of a partition of the continuous time interval  $t \in [0, T]$  into discrete times  $t_k \in \{0 = t_0, t_1, \dots, t_l, t_{l+1}, \dots, t_L = T\}$ , any explicit or implicit time integration scheme can be written in the form

$$\mathbf{Y}_{k+1} = \mathbf{A}_{k+1} \mathbf{Y}_k \quad (26)$$

in terms of the so-called propagator matrix  $\mathbf{A}$ . For example, for the basic cases of explicit and implicit first-order time integration schemes, we have

$$\mathbf{A}_{k+1} = \begin{cases} \mathbf{I} + \Delta t_k \mathbf{M}(t_k, \mathbf{Y}_k) \mathbf{Y}_k^{-1} & \text{(explicit)} \\ \mathbf{I} + \Delta t_k \mathbf{M}(t_{k+1}, \mathbf{Y}_{k+1}) \mathbf{Y}_k^{-1} & \text{(implicit)} \end{cases}, \quad (27)$$

where, again,  $\Delta t_k = t_{k+1} - t_k$ . In general, the approximation provided by (26) is such that  $\det \mathbf{Y}_{k+1} \neq \det \mathbf{Y}_k$  and hence does *not* satisfy the constraint (25)<sub>2</sub>. It turns out that a rather intuitive modification of (26) leads to a scheme that does satisfy the constraint (25)<sub>2</sub> identically. That scheme is

$$\mathbf{Y}_{k+1} = \frac{1}{(\det \mathbf{A}_{k+1})^{1/N}} \mathbf{A}_{k+1} \mathbf{Y}_k, \quad (28)$$

where we emphasize that  $\mathbf{A}_{k+1}$  is any propagator of choice and thus (28) applies to any explicit or implicit time integration scheme of choice.

Provided that  $\det \mathbf{Y}_k = 1$ , it is a simple matter to show that the scheme (28) preserves the constraint (25)<sub>2</sub> identically. What is more, as detailed by the next proposition, the proof of which is provided in the Appendix, the scheme (28) has the added merit of preserving the same order of accuracy as the base time integration scheme.

**Proposition.** [Error Bound for the Proposed Scheme] Denote by  $\mathbf{Y}_{k+1}^{ex}$ ,  $\mathbf{Y}_{k+1}^b$ , and  $\mathbf{Y}_{k+1}$  the exact solution of the system of first-order ODEs (25), the approximate solution (26) generated by a base time integrator, and the approximate solution (28) generated by the associated proposed scheme at time  $t = t_{k+1} \in \{t_1, \dots, t_l, t_{l+1}, \dots, t_L = T\}$ , respectively. Let  $\Delta t = \sum_{k=1}^{L-1} (t_{k+1} - t_k) / (L - 1)$ . If the base time integrator has accuracy of order  $r$ , that is, if

$$\|\mathbf{Y}_{k+1}^b - \mathbf{Y}_{k+1}^{ex}\|_{\infty} \leq \beta \Delta t^r \tag{29}$$

for some  $\beta > 0$ , then, under the technical conditions spelled out in the Appendix, it follows that

$$\|\mathbf{Y}_{k+1} - \mathbf{Y}_{k+1}^{ex}\|_{\infty} \leq \alpha \Delta t^r \tag{30}$$

for some  $\alpha > 0$ .

### 3.7. Numerical experiments illustrating the error bound (30)

The two sets of numerical experiments that follow illustrate the error bound (30) for three different base time integration schemes: forward Euler (fE), backward Euler (bE), and a fifth-order explicit Runge–Kutta (RK5) scheme. The first two are selected because they are of common use and because they typically deliver widely inaccurate determinant of solution for systems of ODEs (25). On the other hand, the RK5 scheme is one of the few schemes that is known to deliver accurate solutions — in particular, such that  $|\det \mathbf{Y}_k^b - 1| = O(\Delta t_k^5)$  — and is included here for completeness.

*Example 1.* Consider first the system of linear first-order ODEs

$$\begin{cases} \dot{\mathbf{Y}} = \mathbf{D}\mathbf{Y}, & t \in (0, T] \\ \det \mathbf{Y} = 1, & t \in [0, T] \\ \mathbf{Y}(0) = \mathbf{Y}_0, \end{cases} \quad \text{with } \mathbf{Y}_0 = \frac{1}{0.18^{1/3}} \begin{bmatrix} 0.8 & -0.2 & -0.4 \\ -0.2 & 0.5 & 1.0 \\ -0.4 & 1.0 & 2.5 \end{bmatrix} \tag{31}$$

for  $\mathbf{Y} \in \mathbb{R}^{3 \times 3}$ , where  $\mathbf{D}$  is a constant matrix. Precisely, we consider the following two cases:

Case 1

$$\mathbf{D} = \begin{bmatrix} -1.7 & 0 & 0 \\ 0 & 0.85 & 0 \\ 0 & 0 & 0.85 \end{bmatrix} \quad \text{and} \quad T = 10.$$

Case 2

$$\mathbf{D} = \begin{bmatrix} 0 & -1 & -1 \\ 1 & 0 & 0 \\ 1 & 0 & 0 \end{bmatrix} \quad \text{and} \quad T = 1.$$

The exact solutions for both of these cases can be determined explicitly. They read

$$\mathbf{Y}^{ex}(t) = \begin{bmatrix} e^{-1.7t} & 0 & 0 \\ 0 & e^{0.85t} & 0 \\ 0 & 0 & e^{0.85t} \end{bmatrix} \mathbf{Y}_0 \quad \text{and} \quad \mathbf{Y}^{ex}(t) = 0.5 \begin{bmatrix} 2 \cos(\sqrt{2}t) & -\sin(\sqrt{2}t) & -\sin(\sqrt{2}t) \\ \sin(\sqrt{2}t) & \cos(\sqrt{2}t) + 1 & \cos(\sqrt{2}t) - 1 \\ \sin(\sqrt{2}t) & \cos(\sqrt{2}t) - 1 & \cos(\sqrt{2}t) + 1 \end{bmatrix} \mathbf{Y}_0, \tag{32}$$

respectively.

Figs. 2, 3, 4, 5 present results for the error measures  $\mathcal{E}_{ij}^b \equiv Y_{ij}^b(T) - Y_{ij}^{ex}(T)$  and  $\mathcal{E}_{ij} \equiv Y_{ij}(T) - Y_{ij}^{ex}(T)$  as functions of the time increment  $\Delta t_k = \Delta t$  for the base schemes bE and RK5 in parts (a) and for the corresponding proposed scheme in parts (b). While Figs. 2 and 3 show results for Case 1, Figs. 4 and 5 show results for Case 2. The corresponding evolution in time  $t$  of  $\det \mathbf{Y}^b$  and  $\det \mathbf{Y}$  for both the base and the proposed schemes are shown in Fig. 6 for various choices of time increments  $\Delta t$ .

Two observations are immediate. First, as expected from the error bound (30), the proposed scheme delivers solutions with the same order of accuracy as the base scheme. Second, the proposed scheme delivers solutions such that  $\det \mathbf{Y} = 1$ , this for any choice of the time increment  $\Delta t$ , even when  $\Delta t$  is considerably large (like for the RK5 results in Fig. 6).

*Example 2.* Consider now the system of nonlinear first-order ODEs

$$\begin{cases} \dot{\mathbf{Y}} = \frac{1}{\tau} \left( \mathbf{D} - \frac{1}{3} (\mathbf{D} \cdot \mathbf{Y}^{-1}) \mathbf{Y} \right), & t \in (0, T] \\ \mathbf{Y}(0) = \mathbf{I}, \end{cases} \tag{33}$$

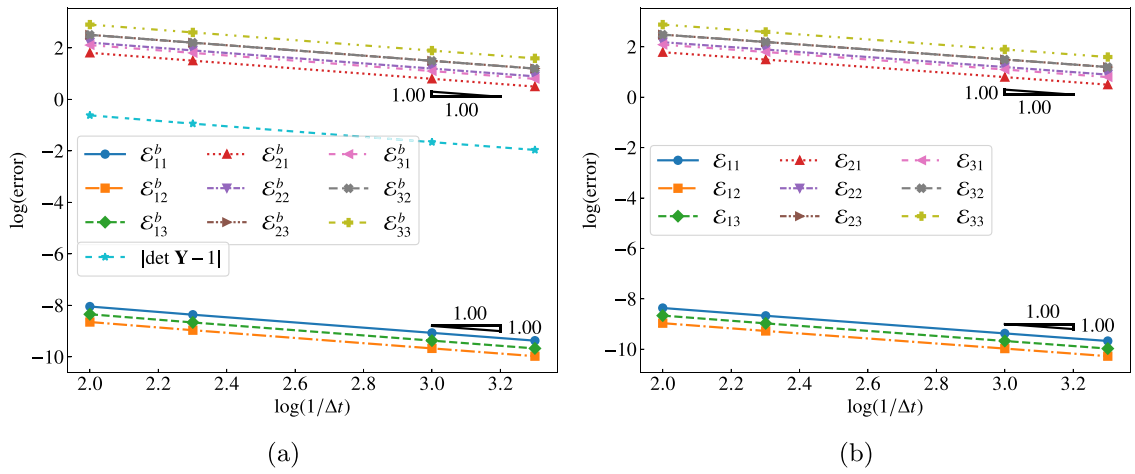


Fig. 2. Case 1: Error convergence of (a) bE and (b) the proposed modified bE.

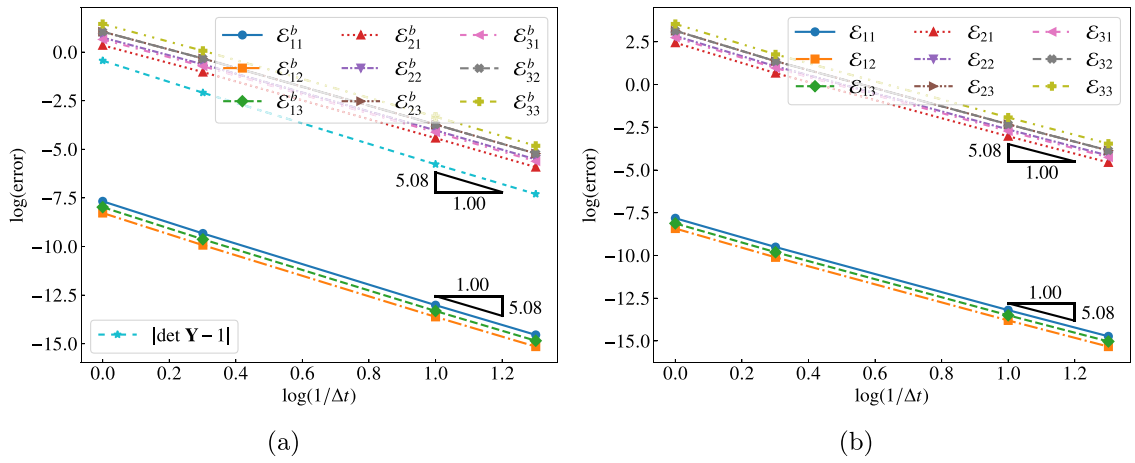


Fig. 3. Case 1: Error convergence of (a) RK5 and (b) the proposed modified RK5.

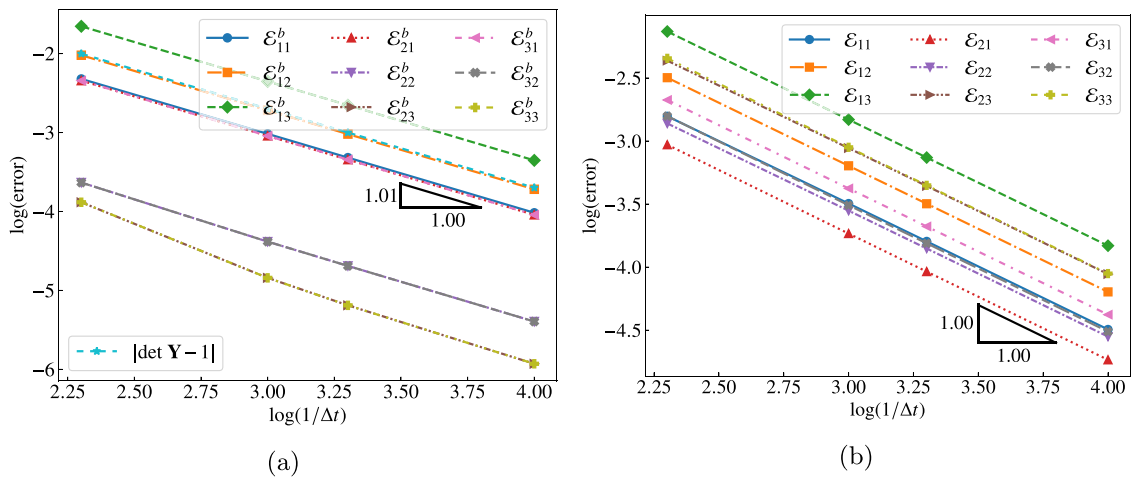


Fig. 4. Case 2: Error convergence of (a) bE and (b) the proposed modified bE.

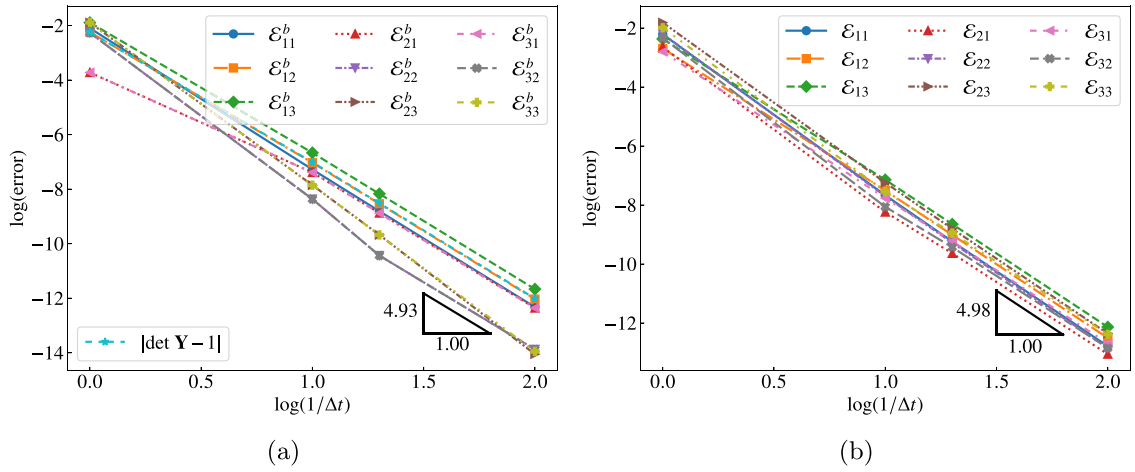


Fig. 5. Case 2: Error convergence of (a) RK5 and (b) the proposed modified RK5.

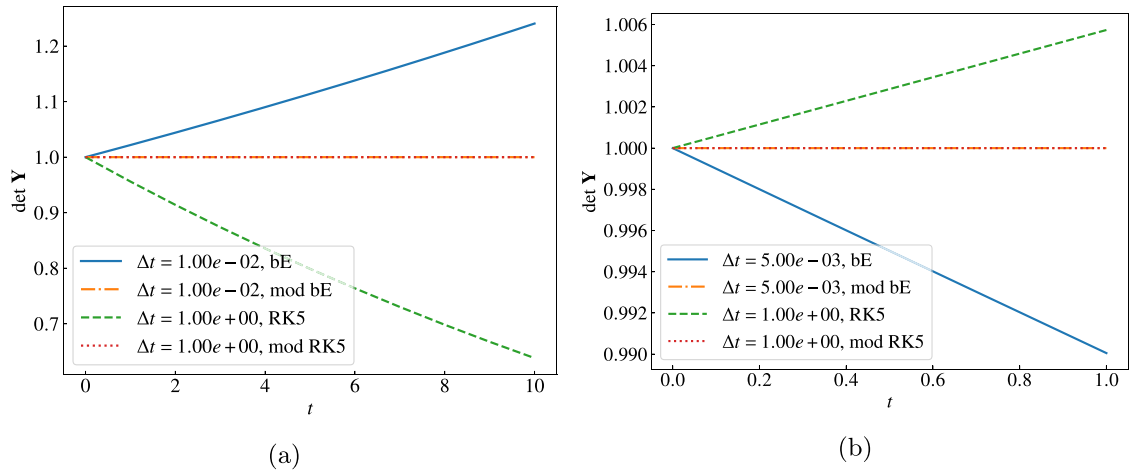


Fig. 6. Evolution in time  $t$  of  $\det \mathbf{Y}^b$  and  $\det \mathbf{Y}$  for (a) Case 1 and (b) Case 2.

for  $\mathbf{Y} \in \mathbb{R}^{3 \times 3}$ , where  $\tau = 1$ ,  $T = 40$ , and  $\mathbf{D}$  is the time-dependent matrix

$$\mathbf{D} = \begin{pmatrix} 1 + \sin^2(2\pi t) & 2 \sin(2\pi t) & 0 \\ 2 \sin(2\pi t) & 1 + \sin^2(2\pi t) & 0 \\ 0 & 0 & 1 \end{pmatrix}. \tag{34}$$

From a mathematical point of view, note that the constraint  $\det \mathbf{Y} = 1$  in (33) is built-in. Physically, the system (33) with forcing term (34) describes the evolution of the viscous part of the deformation in a canonical elastomer with Gaussian elasticity and constant relaxation time  $\tau = 1$  that is subjected to the type of cyclic simple shear applied by a conventional DMA (dynamic mechanical analysis) tester.

Contrary to the previous example, the exact solution of the system (33) with (34) does not admit an explicit form. Nevertheless, it is such that  $\det \mathbf{Y}^{ex} = 1$ . Fig. 7 presents results for the error measure  $|\det \mathbf{Y}^b - 1|$  as a function of the time increment  $\Delta t_k = \Delta t$  for the base scheme fE in part (a) and for the base scheme bE in part (b). The corresponding evolution of  $\det \mathbf{Y}^b$  and  $\det \mathbf{Y}$  in time  $t$  for both the base and the proposed schemes are shown in Figs. 7(c) and (d) for various choices of time increments  $\Delta t$ .

The main observation from these results is that while both the fE and bE schemes exhibit the expected rate of convergence, their accuracy is unacceptably inaccurate, even for considerably small time increments  $\Delta t$ . What is more, this inaccuracy worsens monotonically as time  $t$  increases. By contrast, the proposed scheme delivers solutions with  $\det \mathbf{Y} = 1$ , irrespective of the base time integration scheme.

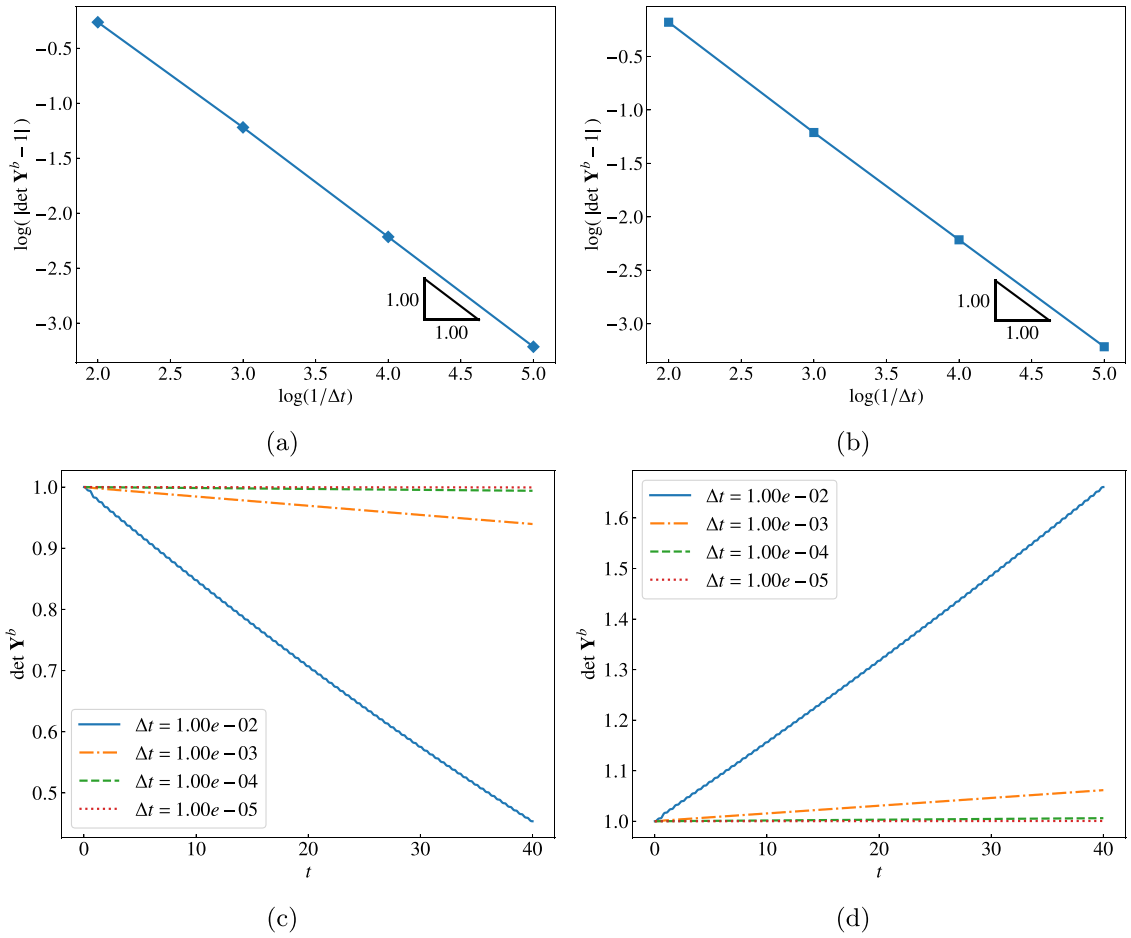


Fig. 7. Error convergence in the measure  $|\det \mathbf{Y}^b - 1|$  of (a) fE and (b) bE. Evolution in time  $t$  of  $\det \mathbf{Y}^b$  and  $\det \mathbf{Y}$  for (c) fE and (d) bE.

#### 4. Sample results

In the sequel, with the objective of showcasing its robustness and wide range of application, we deploy the above-developed formulation to generate solutions for four representative initial-boundary-value problems. We begin in Section 4.1 by considering the uniaxial tensile loading/unloading at various constant stretch rates and the tensile relaxation of VHB 4910, a popular acrylic elastomer from the company 3M. In Section 4.2, we consider the indentation of a block made of two viscoelastic elastomers with widely disparate compressibilities. In Section 4.3, we consider the indentation of a block of a soft biological tissue, porcine liver. Finally, in Section 4.4, we consider the response of a suspension of bubbles in a canonical elastomer with Gaussian elasticity and constant viscosity subjected to simple shear.

In all the simulations that follow, we make use of the compressible version of the constitutive model introduced in Kumar and Lopez-Pamies (2016). Precisely, we take the equilibrium free-energy function (3)<sub>1</sub>, the non-equilibrium free energy function (3)<sub>2</sub>, and the viscosity function (3)<sub>3</sub> to be given by

$$\left\{ \begin{aligned} \psi^{\text{Eq}}(I_1, J) &= \sum_{r=1}^2 \frac{3^{1-a_r}}{2a_r} \mu_r (I_1^{\alpha_r} - 3^{\alpha_r}) - \sum_{r=1}^2 \mu_r \ln J + \frac{\kappa}{2} (J - 1)^2 \\ \psi^{\text{NEq}}(I_1^e, J) &= \sum_{r=1}^2 \frac{3^{1-a_r}}{2a_r} m_r (I_1^{e a_r} - 3^{a_r}) - \sum_{r=1}^2 m_r \ln J + \frac{\kappa}{2} (J - 1)^2 \\ \eta(I_1^e, I_2^e, I_1^v) &= \eta_\infty + \frac{\eta_0 - \eta_\infty + K_1 [I_1^{v \beta_1} - 3^{\beta_1}]}{1 + (K_2 J_2^{\text{NEq}})^{\beta_2}} \quad \text{with } J_2^{\text{NEq}} = \left( \frac{I_1^{e2}}{3} - I_2^e \right) \left( \sum_{r=1}^2 3^{1-a_r} m_r I_1^{e a_r - 1} \right)^2 \end{aligned} \right. ,$$

**Table 1**  
Material constants for VHB 4910.

$\mu_1 = 13.54$ kPa	$\mu_2 = 1.08$ kPa	$\alpha_1 = 1.00$	$\alpha_2 = -2.474$	$\kappa = 2.041 \times 10^6$ kPa
$m_1 = 5.42$ kPa	$m_2 = 20.78$ kPa	$a_1 = -10$	$a_2 = 1.948$	$K_1 = 3507$ kPa s
$\eta_0 = 7014$ kPa s	$\eta_\infty = 0.1$ kPa s	$\beta_1 = 1.852$	$\beta_2 = 0.26$	$K_2 = 1$ kPa <sup>-2</sup>

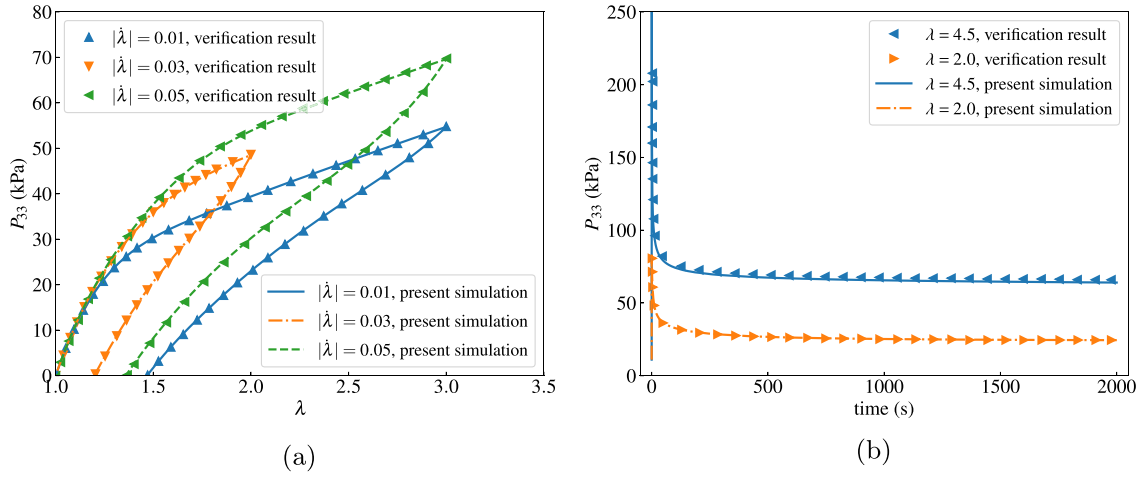


**Fig. 8.** Comparisons with the results in Kumar and Lopez-Pamies (2016) for the response of VHB 4910 under: (a) uniaxial tension loading/unloading at various constant stretch rates and (b) a single-step relaxation with two different applied stretches.

which result in the constitutive relation

$$\mathbf{P}(\mathbf{X}, t) = \sum_{r=1}^2 3^{1-a_r} \mu_r I_1^{\alpha_r-1} \mathbf{F} + \sum_{r=1}^2 3^{1-a_r} m_r I_1^{e a_r-1} \mathbf{F} \mathbf{C}^{v-1} - \left( \sum_{r=1}^2 (3^{1-a_r} \mu_r + 3^{1-a_r} m_r) - 2\kappa(J-1)J \right) \mathbf{F}^{-T} \tag{35}$$

with evolution equation

$$\dot{\mathbf{C}}^v(\mathbf{X}, t) = \frac{\sum_{r=1}^2 3^{1-a_r} m_r (\mathbf{C} \cdot \mathbf{C}^{v-1})^{a_r-1}}{\eta(I_1^e, I_2^e, I_1^v)} \left( \mathbf{C} - \frac{1}{3} (\mathbf{C} \cdot \mathbf{C}^{v-1}) \mathbf{C}^v \right). \tag{36}$$

In all, the constitutive relation (35)–(36) contains fifteen material constants. Four of them,  $\mu_1, \mu_2, \alpha_1, \alpha_2$ , serve to characterize the non-Gaussian elasticity of the elastomer at states of thermodynamic equilibrium. Another four,  $m_1, m_2, a_1, a_2$ , characterize the non-Gaussian elasticity at non-equilibrium states. One of them,  $\kappa$ , serves to characterize the compressibility. The last six constants,  $\eta_0, \eta_\infty, K_1, K_2, \beta_1, \beta_2$ , serve to characterize the nonlinear shear-thinning viscosity. The prescription (35)–(36) has been shown to be accurately descriptive and predictive of a wide range of elastomers, which typically exhibit non-Gaussian elasticity as well as nonlinear viscosity of shear-thinning type (Lopez-Pamies, 2010; Kumar and Lopez-Pamies, 2016; Ghosh and Lopez-Pamies, 2021; Chockalingam et al., 2021; Chen and Ravi-Chandar, 2022), thus its use here.

#### 4.1. Uniaxial tension of the acrylic elastomer VHB 4910

To verify the proposed formulation, we begin by comparing its predications with the results of Kumar and Lopez-Pamies (2016) for the stress–stretch and the stress-time responses of the acrylic elastomer VHB 4910 under uniaxial tension carried out at three different constant stretch rates  $|\dot{\lambda}| = 0.01, 0.03, 0.05 \text{ s}^{-1}$  and under a single-step relaxation with stretches  $\lambda = 2, 4.5$ . The pertinent material constants for VHB 4910 are given in Table 1.

The main technical aspects of the simulations are as follows. Given the homogeneity of the fields in space, we discretize the domain with a single linear hexahedral element. The simulations of the tests at constant stretch rate are performed with the uniform time step  $\Delta t = 0.5$  s. For the relaxation tests, the loading part of the test is taken to last 1 s. During this loading part, we make use of the uniform time step  $\Delta t = 0.01$  s, while  $\Delta t = 1.0$  s is used during the relaxation part. All simulations are carried out with the proposed time integration scheme based on a BE scheme.

The comparisons presented in Fig. 8 indicate that the proposed formulation delivers the correct solutions.

#### 4.2. Indentation of a block made of viscoelastic elastomers with disparate compressibilities

Next, we consider a test problem that has been studied by several authors (Reese et al., 2000; Caylak and Mahnken, 2012; Masud and Truster, 2013), that of a block of material that is loaded with a localized pressure applied at the center of its top boundary.

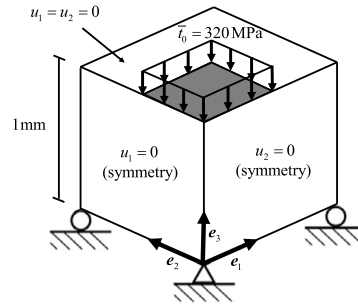


Fig. 9. Schematic of the indentation of a block made of viscoelastic elastomers with disparate compressibilities.

Table 2

Material constants for the highly compressible and the nearly incompressible elastomers with Gaussian elasticity.

$\mu_1 = 20.00$ MPa	$\mu_2 = 10.00$ MPa	$\alpha_1 = 1.00$	$\alpha_2 = 1.00$	$K_1 = 442.00$ MPa s
$m_1 = 20.00$ MPa	$m_2 = 20.00$ MPa	$a_1 = 1.00$	$a_2 = 1.00$	
$\eta_0 = 20.11$ MPa s	$\eta_\infty = 10.10$ MPa s	$\beta_1 = 3.00$	$\beta_2 = 1.93$	$K_2 = 1289.49$ MPa <sup>-2</sup>
highly compressible: $\kappa = 70$ MPa		nearly incompressible: $\kappa = 3.5 \times 10^6$ MPa		

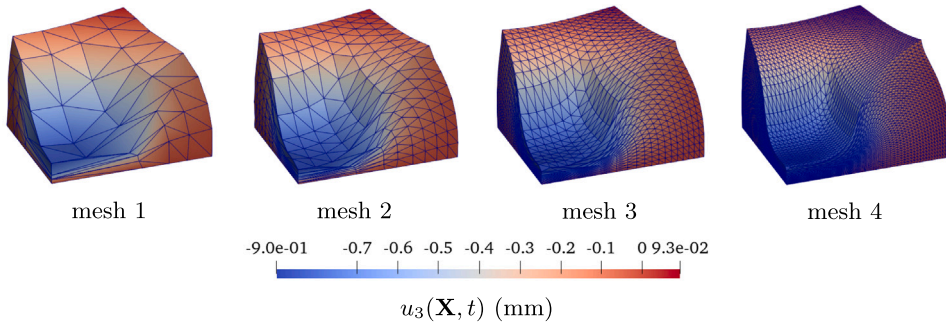


Fig. 10. Contour plots of the displacement field  $u_3(\mathbf{X}, t)$  at  $t = T = 2$  s for T4 elements and several meshes of increasing refinement.

Specifically, as depicted by Fig. 9, exploiting symmetry, we consider a (quarter of a) cube with dimensions  $1 \text{ mm} \times 1 \text{ mm} \times 1 \text{ mm}$  in its undeformed configuration. A nominal traction  $\bar{\mathbf{t}} = -\bar{t} \mathbf{e}_3$  is applied, first linearly in time over  $0.1$  s until reaching the value  $\bar{t} = \bar{t}_0 = 320$  MPa after which point the traction is held constant for  $2$  s, at its top boundary  $X_3 = 1$  mm over the central region  $0 < X_1 < 0.5$  mm,  $0 < X_2 < 0.5$  mm. For the constitutive behavior of the material, we consider the cases of two viscoelastic elastomers with Gaussian elasticity, one highly compressible, the other nearly incompressible. The pertinent material constants for both of them are listed in Table 2.

The main technical aspects of the simulations are as follows. We discretize the cube into a conforming structured grid such that the edges are divided into 4,8,16, and 32 segments. The smaller subcube in the grid is discretized with 6 linear tetrahedral (T4) elements or a single hexahedral (H8) element. All simulations are carried out with the proposed time integration scheme based on a bE scheme and a RK5 scheme and with the uniform time increment  $\Delta t = 0.01$  s. Also, unless otherwise noted, all results pertain to the nearly-incompressible case where the domain is discretized into the finest H8 elements (mesh 4) and the evolution equations are solved using the proposed modified bE and modified RK5 schemes up to the total time of  $T = 2$  s.

Figs. 10 and 11 show contour plots of the displacement field  $u_3(\mathbf{X}, t)$  over the deformed configuration at the final instance  $t = T = 2$  s of the applied loading for T4 and H8 elements and four meshes of increasing refinement. It is plain that there are no locking problems for either type of element.

Figs. 12 and 13 present results for the volume average of  $\det \mathbf{C}$  over an octant of the cube directly below the applied load for several combinations of compressibility, element type, mesh refinement, and choice of time integration scheme. There are two key observations from these results. First, consistent with the exact solution,  $\det \mathbf{C}^v \rightarrow 1$  for the nearly incompressible elastomer as the mesh is refined. Second, the same formulation is able to deliver converged solutions for both a nearly incompressible elastomer as well as a highly compressible one, irrespective of the element type and choice of base scheme for the time integration.

Figs. 14 and 15 show contour plots of  $\det \mathbf{C}^v$  over the deformed configuration at the final instance  $t = T = 2$  s of the applied loading for T4 and H8 elements. For direct comparison, parts (a) show the results obtained with the bE scheme and parts (b) show the results obtained with the corresponding proposed time integration scheme. It is plain that the proposed scheme delivers solutions with  $\det \mathbf{C}^v = 1$ . The same is *not* true for the bE scheme, which in fact leads to highly inaccurate solutions.

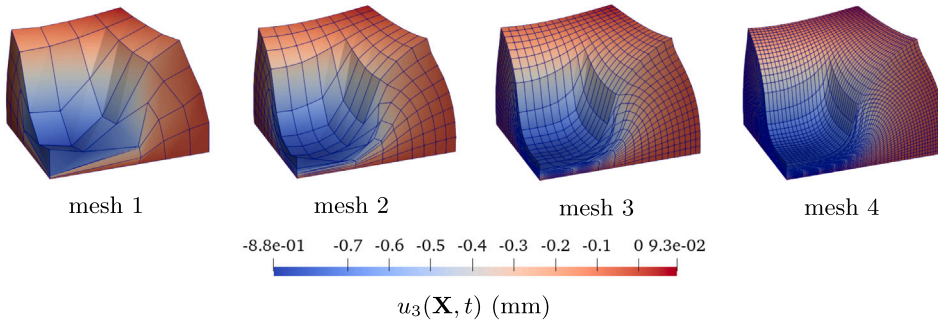


Fig. 11. Contour plots of the displacement field  $u_3(\mathbf{X}, t)$  at  $t = T = 2$  s for H8 elements and several meshes of increasing refinement.

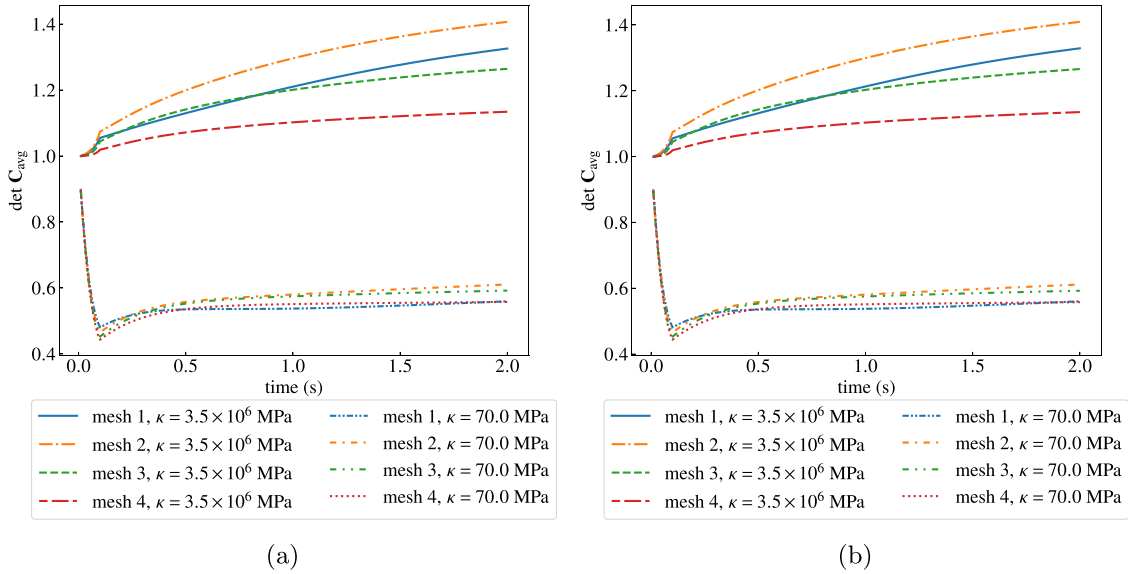


Fig. 12. Evolution in time  $t$  of  $\det \mathbf{C}$  averaged over an octant of the cube directly below the applied load for T4 elements and the proposed time integration scheme with base scheme (a) bE and (b) RK5.

**Table 3**  
Material constants for porcine liver.

$\mu_1 = 0.34$ kPa	$\mu_2 = 0.00$ kPa	$\alpha_1 = 1.00$	$\alpha_2 = 1.00$	$\kappa = 8.15 \times 10^4$ kPa
$m_1 = 0.14$ kPa	$m_2 = 0.00$ kPa	$a_1 = 1.00$	$a_2 = 1.00$	$K_1 = 3507$ kPa s
$\eta_0 = 10^{-2}$ kPa s	$\eta_\infty = 10^{-3}$ kPa s	$\beta_1 = 0.28$	$\beta_2 = 0.45$	$K_2 = 1000$ kPa $^{-2}$

Finally, Fig. 16 presents results for the evolution in time  $t$  of  $\det \mathbf{C}^v$  at the integration point closest to  $(X_1, X_2, X_3) = (0, 0, 0.5)$  mm for T4 and H8 elements and base and modified bE and RK5 time integration schemes. Consistent with all the preceding results, the modified schemes are again seen to satisfy the constraint  $\det \mathbf{C}^v = 1$  exactly.

### 4.3. Indentation of porcine liver

In this subsection, we deploy the proposed formulation to simulate an indentation experiment on porcine liver reported in Ahn and Kim (2010). We focus on the experiment, carried out with a cylindrical indenter of 10 mm diameter and hemisphere shaped tip, in which an indentation depth of 5 mm is rapidly reached in 0.3125 s and then the force relaxation is measured over 50 s; see Fig. 6(b) in Ahn and Kim (2010).

In the simulation, as illustrated by Fig. 17, we model the specimen as a cylinder of height 50 mm and diameter 150 mm in its initial configuration. The bottom of the cylinder is held fixed and the deformation applied by the indenter is modeled directly as a Dirichlet boundary condition. By exploiting symmetry, as also illustrated by Fig. 17, we only model explicitly a quarter of the cylinder and apply the pertinent boundary conditions on the planes of symmetry. We discretize the specimen with linear hexahedral elements. The result included here corresponds to a mesh with 24150 elements and is generated with the proposed time integration

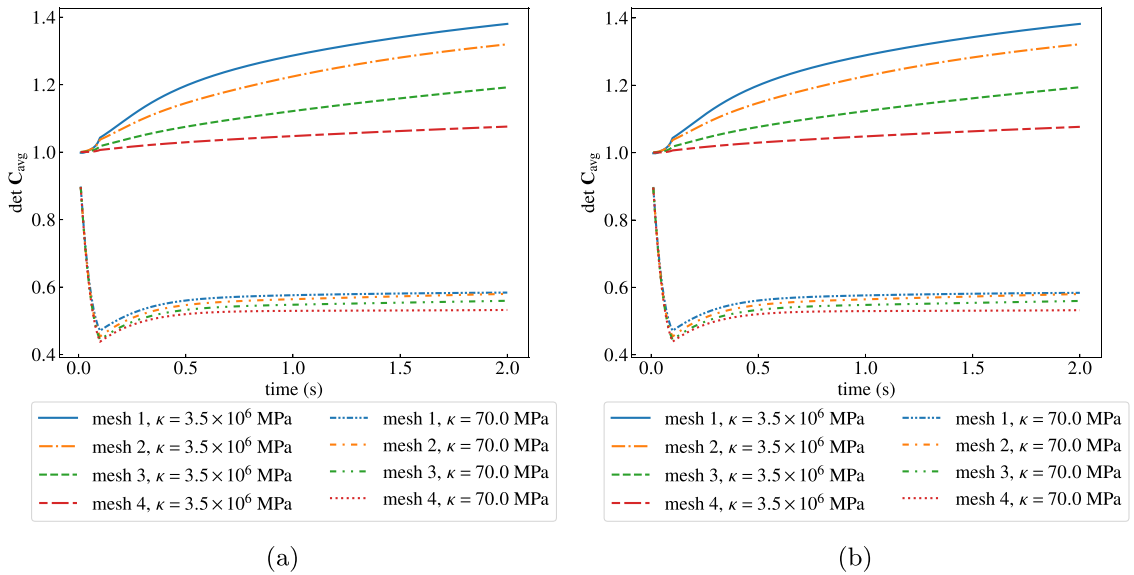


Fig. 13. Evolution in time  $t$  of  $\det \mathbf{C}$  averaged over an octant of the cube directly below the applied load for H8 elements and the proposed time integration scheme with base scheme (a) bE and (b) RK5.

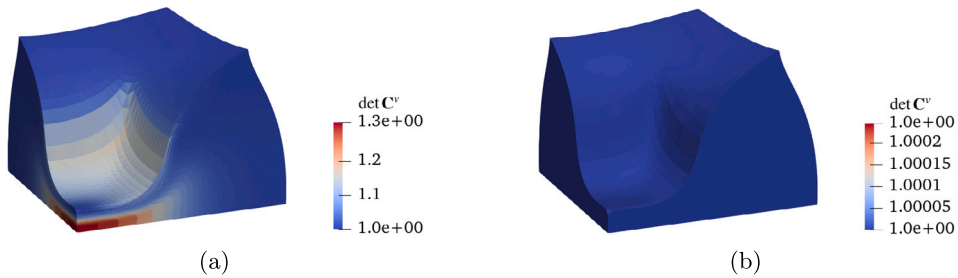


Fig. 14. Contour plots of  $\det \mathbf{C}^v$  over the deformed configuration at the final instance  $t = T = 2$  s of the applied loading for T4 elements. The results are shown for (a) the bE scheme and (b) the proposed modified bE scheme.

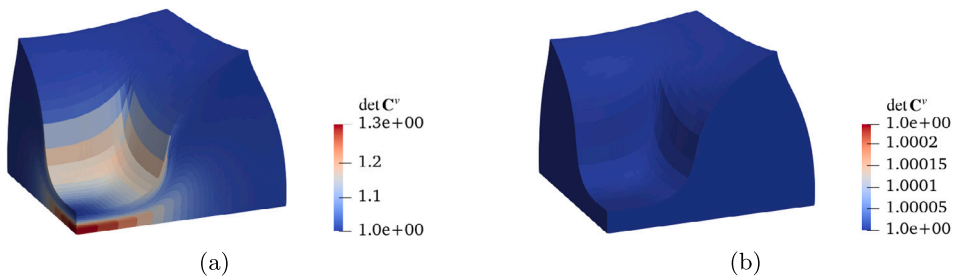


Fig. 15. Contour plots of  $\det \mathbf{C}^v$  over the deformed configuration at the final instance  $t = T = 2$  s of the applied loading for H8 elements. The results are shown for (a) the bE scheme and (b) the proposed modified bE scheme.

scheme based on a RK5 scheme. The material parameters used in the simulation are obtained by fitting the constitutive model (35)–(36) to the relaxation data reported in Ahn and Kim (2010). They are listed in Table 3. From these parameters we can readily deduce that porcine liver is extremely soft and that it exhibits shear-thinning viscosity. At any rate, we should remark here that the data reported in Ahn and Kim (2010) is not sufficient to carry out an accurate fitting of all the material constant in (35)–(36). For the representative purposes of this subsection, however, the constants in Table 3 are enough.

Fig. 18 compares the force-time predicted by the proposed formulation with the experimental data in Ahn and Kim (2010). For completeness, the plot also includes the simulation reported in Ahn and Kim (2010). As for the previous sample problems, here too the proposed formulation is able to deliver a stable and accurate solution.

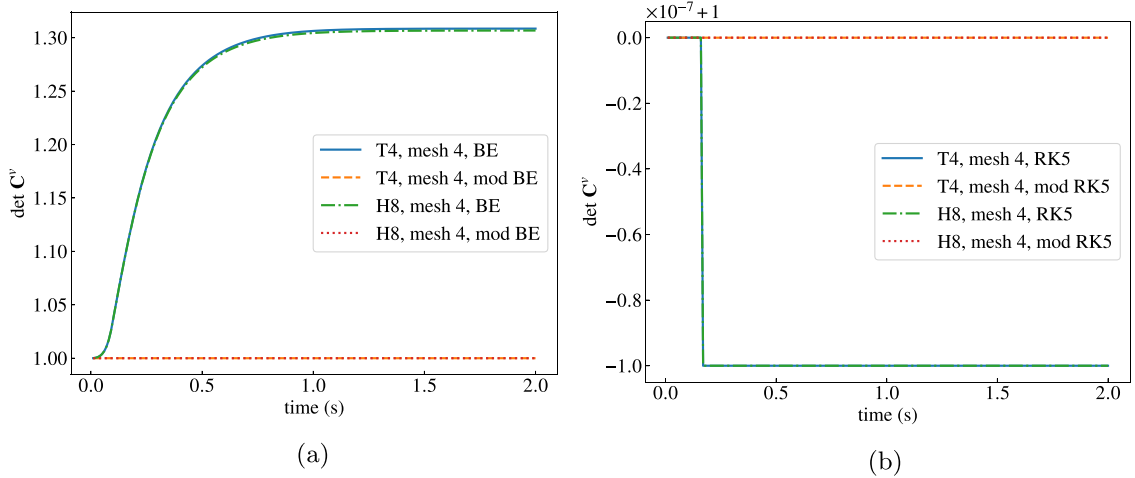


Fig. 16. Evolution in time of  $\det C^v$  at the integration point closet to  $(X_1, X_2, X_3) = (0, 0, 0.5)$  mm. The results are shown for (a) the bE and the proposed modified bE schemes and for (b) the RK5 and the proposed modified RK5 schemes.

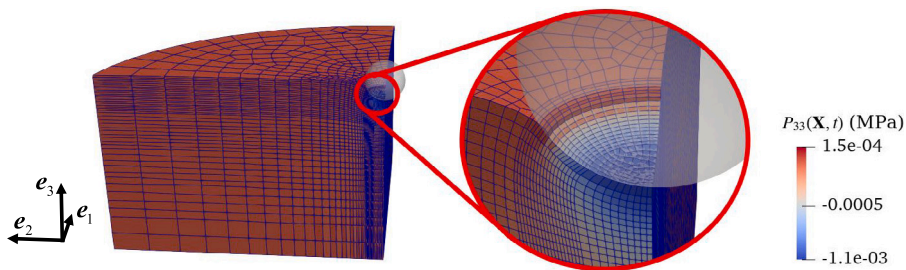


Fig. 17. Geometry of the specimen, mesh, and contour plot of the first Piola-Kirchhoff stress  $P_{33}(X, t)$  over the deformed configuration at the final time  $t = T = 50$  s of the applied loading.

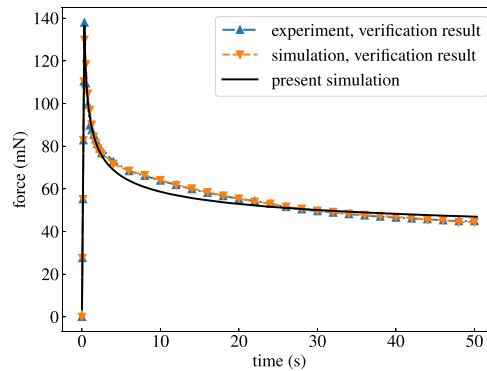


Fig. 18. Comparison of the force-time response predicted by the simulation with the indentation experimental data and simulation reported in Ahn and Kim (2010) for porcine liver.

#### 4.4. The macroscopic response of a suspension of spherical bubbles in a viscoelastic elastomer

In this final subsection, we deploy the proposed formulation to simulate the macroscopic response of a random isotropic suspension of vacuous bubbles in a canonical elastomer with Gaussian elasticity and constant viscosity subjected to simple shear, a problem that has been recently considered in Shrimali et al. (2021).

Specifically, as depicted by Fig. 19, we consider a cube with dimensions  $1 \text{ cm} \times 1 \text{ cm} \times 1 \text{ cm}$  in its undeformed configuration that contains a random isotropic suspension of 200 initially spherical bubbles, all of the same monodisperse size, at volume fraction  $c = 0.15$ , constructed by the well-settled method of Lubachevsky et al. (1991). On its boundary, the cube is subjected to the affine

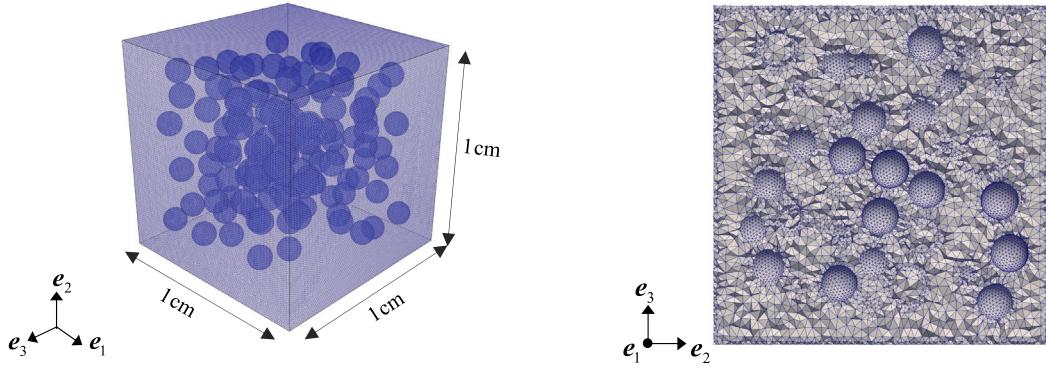


Fig. 19. Specimen containing 200 randomly distributed initially spherical bubbles of monodisperse size at volume fraction  $c = 0.15$  and its FE discretization with approximately 1.4 million linear tetrahedral (T4) elements.

Table 4

Material constants for the canonical elastomer embedding the bubbles.

$\mu_1 = 0.05$ MPa	$\mu_2 = 0$	$\alpha_1 = 1$	$\alpha_2 = 0$	$\kappa = 10^4$ MPa
$m_1 = 25$ MPa	$m_2 = 0$	$a_1 = 1$	$a_2 = 0$	$K_1 = 0$
$\eta_0 = 5$ MPa s	$\eta_\infty = 0$	$\beta_1 = 0$	$\beta_2 = 0$	$K_2 = 0$

simple shear deformation  $\bar{\varphi}(\mathbf{X}, t) = \bar{\mathbf{F}}(t)\mathbf{X}$  with  $\bar{\mathbf{F}}(t) = \mathbf{I} + \bar{F}_{12}(t)\mathbf{e}_1 \otimes \mathbf{e}_2$  and  $\bar{F}_{12}(t) = t^2/k$ ,  $k = 12.5$  s<sup>2</sup>. The bubbles are taken to be vacuous, while the elastomer, again, is taken to be canonical with the material constants given in Table 4.

The main technical aspects of the simulations are as follows. We make use of the open-source mesh generator code Netgen (Schöberl, 1997) to discretize the constructed suspension with nonoverlapping linear tetrahedral (T4) elements. The results presented here correspond to a mesh with about 1.4 million elements, which was checked to be sufficiently refined to deliver accurate solutions. The simulation is performed with the uniform time step  $\Delta t = 0.01$  s. The evolution equations are solved using the proposed modified fE scheme up to the total time of  $T = 6.25$  s.

Fig. 20 presents results for the average Cauchy shear stress

$$\bar{T}_{12} := \frac{1}{|\Omega(t)|} \int_{\Omega(t)} T_{12}(\mathbf{x}, t) dx, \quad \mathbf{T} = \mathbf{J}^{-1} \mathbf{P} \mathbf{F}^T,$$

as a function of the applied Eulerian shear strain rate

$$\bar{D}_{12} = \frac{\dot{t}}{k}, \quad \bar{\mathbf{D}} := \frac{1}{2} \left( \dot{\bar{\mathbf{F}}} \bar{\mathbf{F}}^{-1} + \bar{\mathbf{F}}^{-T} \dot{\bar{\mathbf{F}}}^T \right).$$

For direct comparison, Fig. 20 includes the corresponding result (dashed line) for the underlying elastomer without the bubbles. From a physical point of view, the results show that the stress–strain-rate response of the suspension exhibits an effective nonlinear viscosity of shear-thinning type, this in spite of the fact that the viscosity of the elastomer is constant. This effective nonlinearity is a direct consequence of the interaction among the bubbles which leads to an overall viscosity that is non-Newtonian (Shrimali et al., 2021). From a computational point of view, moreover, the results show that the proposed formulation, yet again, is able to deliver stable and accurate solutions when using low-order space and time approximations, even for challenging homogenization problems.

## 5. Concluding remarks

In this paper, we have presented a internal-variable-based formulation and associated numerical scheme to describe the mechanical response of a large class of viscoelastic bodies undergoing finite quasistatic deformations.

A distinguishing feature of the proposed formulation is that, by making use of a suitably defined partial Legendre transform, it applies to bodies of any compressibility, from the very compressible, to the nearly incompressible, to the fully incompressible. The governing equations amount to the system of PDEs (14) coupled with the ODEs (15) for the deformation field  $\varphi(\mathbf{X}, t)$ , the pressure field  $p(\mathbf{X}, t)$ , and the internal variable  $\mathbf{C}^v(\mathbf{X}, t)$ .

The proposed numerical scheme makes use of a VMS FE discretization of space and of a FD discretization of time together with a new time integration scheme. On one hand, the stabilization imparted by the VMS approach allows to make use of any combination of choice for the shape functions approximating the deformation and the pressure fields. In particular, it allows to use shape functions of low order. On the other hand, the new time integration scheme (28) allows to convert any explicit or implicit time integration scheme of any order into a stable scheme that preserves the constraint  $\det \mathbf{C}^v(\mathbf{X}, t) = 1$  on the internal variable identically. This flexibility in permitting the use of low-order discretizations is expected to significantly improve the existing approach to finite viscoelastostatics in the literature, which is based on higher-order discretizations that are computationally more costly.

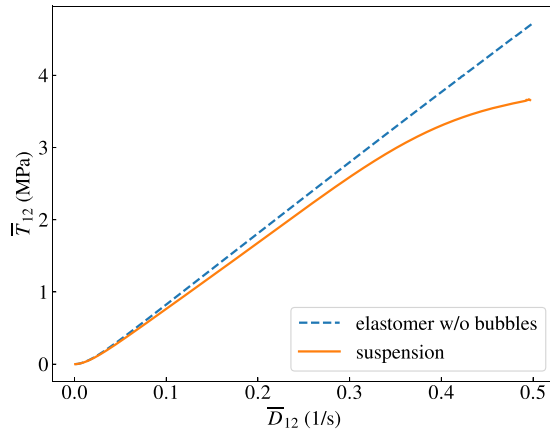


Fig. 20. Response of the suspension of bubbles under simple shear. The plots show the resulting average Cauchy shear stress  $\bar{T}_{12}$  as a function of the applied Eulerian shear rate  $\bar{D}_{12}$ . For direct comparison, the plot includes the corresponding response (dashed line) of the underlying elastomer without the bubbles.

Through its application to four different sample initial–boundary-value problems, we have demonstrated that the proposed numerical method is indeed able to handle realistically complex problems in a robust and efficient manner. In particular, the scheme has been implemented in 3D using low-order 4-node tetrahedral and 8-node hexahedral elements in space, in conjunction with low-order forward- and backward-Euler schemes, as well as a high-order explicit Runge–Kutta scheme, in time.

**Declaration of competing interest**

The authors declare that they have no known competing financial interests or personal relationships that could have appeared to influence the work reported in this paper.

**Data availability**

Data will be made available on request.

**Acknowledgments**

I.P.A. Wijaya and A. Masud were partly supported by NIH, United States Grant No. R01GM135921. The work of O. Lopez-Pamies was supported by the National Science Foundation, United States through the Grant CMMI-1901583.

**Appendix. Proof of the error bound (30)**

In this appendix, we provide a proof of the error bound (30). Throughout, we assume that  $\mathbf{Y}^{ex}$  and  $\mathbf{Y}^b$  are positive definite,  $\prod_{i=1}^{k+1} \det \mathbf{A}_i > 0$ , and make use of the notation

$$\|\mathbf{Y}\|_\infty = \max_{1 \leq i, j \leq N} |Y_{ij}|,$$

where  $Y_{ij}$  are the entries of the matrix  $\mathbf{Y}$ ; recall that  $\mathbf{A}_{k+1}$  denotes the propagator matrix of a base time integration scheme of accuracy order  $r$ .

**Lemma 1.** For some  $\beta_1 > 0$ ,

$$\prod_{i=1}^{k+1} \det \mathbf{A}_i \leq 1 + \beta_1 \Delta t^r. \tag{37}$$

**Proof.** Noting that, for some constant positive-definite matrix  $\mathbf{H} \in \mathbb{R}^{N \times N}$ ,

$$\left( \prod_{i=1}^{k+1} \mathbf{A}_i \right) \mathbf{Y}_0^{ex} - \mathbf{Y}_{k+1}^{ex} \leq \Delta t^r \mathbf{H}$$

and using the positive-definiteness of  $\mathbf{Y}_{k+1}^{ex}$  and  $\mathbf{Y}_{k+1}^b$ , we have

$$\left( \prod_{i=1}^{k+1} \det \mathbf{A}_i \right) \det \mathbf{Y}_0^{ex} \leq \det \mathbf{Y}_{k+1}^{ex} \det (\mathbf{I} + \Delta t^r \mathbf{H} \mathbf{Y}_{k+1}^{ex-1}).$$

Using the fact that  $\det \mathbf{Y}_0^{ex} = \det \mathbf{Y}_{k+1}^{ex}$ , together with the elementary identity  $\det(\mathbf{I} + \epsilon \mathbf{H}) = 1 + \text{tr} \mathbf{H} \epsilon + O(\epsilon^2)$ , the inequality (37) follows.  $\square$

**Lemma 2.** For some  $\beta_2 > 0$ ,

$$1 - \beta_2 \Delta t^r \leq \left( \prod_{i=1}^{k+1} \det \mathbf{A}_i \right). \tag{38}$$

**Proof.** Noting that, for some constant positive-definite matrix  $\mathbf{H} \in \mathbb{R}^{N \times N}$ ,

$$-\Delta t^r \mathbf{H} \leq \left( \prod_{i=1}^{k+1} \mathbf{A}_i \right) \mathbf{Y}_0^{ex} - \mathbf{Y}_{k+1}^{ex}$$

and using the positive-definiteness of  $\mathbf{Y}_{k+1}^{ex}$  and  $\mathbf{Y}_{k+1}^b$ , we have

$$\det \mathbf{Y}_{k+1}^{ex} \leq \det \left( \left( \prod_{i=1}^{k+1} \mathbf{A}_i \right) \mathbf{Y}_0^{ex} + \Delta t^r \mathbf{H} \right).$$

Using the fact that  $\det \mathbf{Y}_{k+1}^{ex} = \det \mathbf{Y}_0^{ex}$ , we further have that

$$\det \mathbf{Y}_0^{ex} \det \mathbf{H}^{-1} \leq \det \left( \left( \prod_{i=1}^{k+1} \mathbf{A}_i \right) \mathbf{Y}_0^{ex} \mathbf{H}^{-1} + \Delta t^r \mathbf{I} \right). \tag{39}$$

Upon employing Theorem 2.3 in Ipsen and Rehman (2008),

$$\det \left( \left( \prod_{i=1}^{k+1} \mathbf{A}_i \right) \mathbf{Y}_0^{ex} \mathbf{H}^{-1} + \Delta t^r \mathbf{I} \right) = \det(\Delta t^r \mathbf{I}) + \det \mathbf{N} + D_1 + D_2 + \dots + D_{N-1} \tag{40}$$

with

$$D_n = \sum_{1 < i_1 < i_2 < \dots < i_n < N} \Delta t^{nr} \det(\mathbf{N}_{i_1 \dots i_n}),$$

where  $\mathbf{N}_{i_1 \dots i_n}$  is the principal submatrix of order  $N - n$  obtained by deleting the row and column  $i_1 \dots i_n$  of the  $N \times N$  matrix

$$\mathbf{N} = \left( \prod_{i=1}^{k+1} \mathbf{A}_i \right) \mathbf{Y}_0^{ex} \mathbf{H}^{-1}.$$

Notice that

$$\det(\Delta t^r \mathbf{I}) + D_1 + D_2 + \dots + D_{N-1} = O(\Delta t^r). \tag{41}$$

Upon substitution of (40) and (41) in (39), we obtain (38).  $\square$

**Corollary 1.**

$$\left( \prod_{i=1}^{k+1} \det \mathbf{A}_i \right) - 1 = O(\Delta t^r).$$

**Proof.** It follows immediately from Lemma 1 and Lemma 2 that

$$-\beta \Delta t^r \leq \left( \prod_{i=1}^{k+1} \det \mathbf{A}_i \right) - 1 \leq \beta \Delta t^r,$$

where  $\beta = \max\{\beta_1, \beta_2\}$ .  $\square$

**Corollary 2.**

$$\left( \prod_{i=1}^{k+1} \det \mathbf{A}_i^{-1/N} \right) - 1 = O(\Delta t^r).$$

**Proof.** Consider the following function

$$f(x) = x^{-1/N}.$$

Using Taylor's formula with remainder,

$$f(x) = f(1) + f'(c)(x - 1)$$

for  $x > 0$  and some  $c$  between 1 and  $x$ . Evaluating the function at  $\left(\prod_{i=1}^{k+1} \det \mathbf{A}_i\right)$  and making use of the assumption  $\left(\prod_{i=1}^{k+1} \det \mathbf{A}_i\right) > 0$ ,

$$\left(\prod_{i=1}^{k+1} \det \mathbf{A}_i^{-1/N}\right) = 1 + f'(c) \left(\left(\prod_{i=1}^{k+1} \det \mathbf{A}_i\right) - 1\right).$$

This, combined with Corollary 1 leads to the result.  $\square$

**Lemma 3.** For some  $\gamma > 0$ ,

$$\|\mathbf{Y}_{k+1} - \mathbf{Y}_{k+1}^b\|_{\infty} \leq \gamma \Delta t^r.$$

**Proof.** Upon noticing that

$$\|\mathbf{Y}_{k+1} - \mathbf{Y}_{k+1}^b\|_{\infty} = \left\| \left( \left[ \prod_{i=1}^{k+1} \det \mathbf{A}_i^{-1/N} \right] - 1 \right) \left( \prod_{i=1}^{k+1} \mathbf{A}_i \right) \mathbf{Y}_0^{\text{ex}} \right\|_{\infty} = \left| \left( \prod_{i=1}^{k+1} \det \mathbf{A}_i^{-1/N} \right) - 1 \right| \|\mathbf{Y}_{k+1}^b\|_{\infty},$$

the result follows immediately from Corollary 2.  $\square$

At this stage, we have all the required background results to prove the error bound (30). Indeed, it follows from the triangle inequality that

$$\|\mathbf{Y}_{k+1} - \mathbf{Y}_{k+1}^{\text{ex}}\|_{\infty} \leq \|\mathbf{Y}_{k+1} - \mathbf{Y}_{k+1}^b\|_{\infty} + \|\mathbf{Y}_{k+1}^b - \mathbf{Y}_{k+1}^{\text{ex}}\|_{\infty}.$$

In turn, the error bound (30) follows immediately from Lemma 3.

## References

- Ahn, B., Kim, J., 2010. Measurement and characterization of soft tissue behavior with surface deformation and force response under large deformations. *Med. Image Anal.* 14, 138–148.
- Anand, M., Kwack, J., Masud, A., 2013. A new generalized Oldroyd-B model for blood flow in complex geometries. *Internat. J. Engrg. Sci.* 72, 78–88.
- Arruda, E.M., Boyce, M.C., 1993. A three-dimensional constitutive model for the large stretch behavior of rubber elastic materials. *J. Mech. Phys. Solids* 41, 389–412.
- Beatty, M.F., 2003. An average-stretch full-network model for rubber elasticity. *J. Elasticity* 70, 65–86.
- Bergstrom, J.S., Boyce, M.C., 1998. Constitutive modeling of the large strain time-dependent behavior of elastomers. *J. Mech. Phys. Solids* 46, 931–954.
- Birzle, A.M., Wall, W.A., 2019. A viscoelastic nonlinear compressible material model of lung parenchyma — Experiments and numerical identification. *J. Mech. Behav. Biomed. Mater.* 94, 164–175.
- Budday, S., Sommer, G., Haybaeck, J., Steinmann, P., Holzapfel, G.A., Kuhl, E., 2017. Rheological characterization of human brain tissue. *Acta Biomater.* 60, 315–329.
- Caylak, I., Mahnken, R., 2012. Stabilization of mixed tetrahedral elements at large deformations. *Int. J. Numer. Methods Eng.* 90, 218–242.
- Chen, S., Ravi-Chandar, K., 2022. Nonlinear poroviscoelastic behavior of gelatin-based hydrogel. *J. Mech. Phys. Solids* 158, 104650.
- Chockalingam, S., Roth, C., Henzel, T., Cohen, T., 2021. Probing local nonlinear viscoelastic properties in soft materials. *J. Mech. Phys. Solids* 146, 104172.
- Croom, B.P., Jin, H., Carroll, J., Long, K., Li, X., 2019. Damage mechanisms in elastomeric foam composites: Multiscale X-ray computed tomography and finite element analyses. *Compos. Sci. Technol.* 169, 195–202.
- Eleni, P.N., Perivoliotis, D., Dragatogiannis, D.A., Krokida, M.K., Polyzois, G.L., Charitidis, C.A., Ziomas, I., Gettleman, L., 2013. Tensile and microindentation properties of maxillofacial elastomers after different disinfecting procedures. *J. Mech. Behav. Biomed. Mater.* 28, 147–155.
- Freed, A.D., Rajagopal, K.R., 2016. A viscoelastic model for describing the response of biological fibers. *Acta Mech.* 227, 3367–3380.
- Gent, A.N., 1996. A new constitutive relation for rubber. *Rubber Chem. Technol.* 69, 59–61.
- Ghosh, K., Lopez-Pamies, O., 2021. On the two-potential constitutive modeling of dielectric elastomers. *Meccanica* 56, 1505–1521.
- Ghosh, K., Shrivali, B., Kumar, A., Lopez-Pamies, O., 2021. The nonlinear viscoelastic response of suspensions of rigid inclusions in rubber: I — Gaussian rubber with constant viscosity. *J. Mech. Phys. Solids* 154, 104544.
- Green, A.E., Rivlin, R.S., 1957. The mechanics of non-linear materials with memory: Part I. *Arch. Ration. Mech. Anal.* 1, 1–21.
- Halphen, B., Nguyen, Q.S., 1975. Sur les matériaux standard généralisés. *J. Méc.* 14, 39–63.
- Hochbruck, M., Ostermann, A., 2010. Exponential integrators. *Acta Numer.* 31, 209–286.
- Hosseini-Farid, M., Ramzanpour, M., Ziejewski, M., Karami, G., 2019. A compressible hyper-viscoelastic material constitutive model for human brain tissue and the identification of its parameters. *Int. J. Non-Linear Mech.* 116, 147–154.
- Idiart, M.I., Lopez-Pamies, O., 2012. On the overall response of elastomeric solids with pressurized cavities. *C. R. Mecanique* 340, 359–368.
- Ipsen, I.C.F., Rehman, R., 2008. Perturbation bounds for determinants and characteristic polynomials. *SIAM J. Matrix Anal. Appl.* 30, 762–776.
- Krieger, I.M., 1972. Rheology of monodisperse latices. *Adv. Colloid Interface Sci.* 3, 111–136.
- Kumar, A., Lopez-Pamies, O., 2016. On the two-potential constitutive modelling of rubber viscoelastic materials. *C. R. Mecanique* 344, 102–112.
- Kwack, J., Masud, A., 2010. A three-field formulation for incompressible viscoelastic fluids. *Internat. J. Engrg. Sci.* 48, 1413–1432.
- Kwack, J., Masud, A., Rajagopal, K.R., 2017. Stabilized mixed three-field formulation for a generalized incompressible Oldroyd-B model: Stabilized mixed method for a generalized Oldroyd-B model. *Internat. J. Numer. Methods Fluids* 83, 704–734.
- Lawson, J.D., 1966. An order five Runge-Kutta process with extended region of stability. *SIAM J. Numer. Anal.* 3, 593–597.
- Le Tallec, P., Rahier, C., Kaiss, A., 1993. Three-dimensional incompressible viscoelasticity in large strains: formulation and numerical approximation. *Comput. Methods Appl. Mech. Engrg.* 109, 233–258.
- Lockett, F.J., 1972. *Nonlinear Viscoelastic Solids*. Academic Press, London, New York.
- Lopez-Pamies, O., 2010. A new  $I_1$ -based hyperelastic model for rubber elastic materials. *C. R. Mecanique* 338, 3–11.
- Lubachevsky, B.D., Stillinger, F.H., Pinson, E.N., 1991. Disks vs spheres: Contrasting properties of random packings. *J. Stat. Phys.* 64, 501–523.
- Mao, Y., Lin, S., Zhao, X., Anand, L., 2017. A large deformation viscoelastic model for double-network hydrogels. *J. Mech. Phys. Solids* 100, 103–130.
- Masud, A., Truster, T.J., 2013. A framework for residual-based stabilization of incompressible finite elasticity: Stabilized formulations and  $\mathbf{F}$  methods for linear triangles and tetrahedra. *Comput. Methods Appl. Mech. Engrg.* 267, 359–399.
- Oyen, M.L., Cook, R.F., 2003. Load-displacement behavior during sharp indentation of viscous-elastic-plastic materials. *J. Mater. Res.* 18, 139–150.

- Pipkin, A.C., Rogers, T.G., 1968. A non-linear integral representation for viscoelastic behaviour. *J. Mech. Phys. Solids* 16, 59–72.
- Reese, S., Govindjee, S., 1998. A theory of finite viscoelasticity and numerical aspects. *Int. J. Solids Struct.* 35, 3455–3482.
- Reese, S., Wriggers, P., Reddy, B.D., 2000. New locking-free brick element technique for large deformation problems in elasticity. *Comput. Struct.* 75, 291–304.
- Schöberl, J., 1997. Netgen an advancing front 2d/3d-mesh generator based on abstract rules. *Comput. Visual. Sci.* 1, 41–52.
- Shrimali, B., Ghosh, K., Lopez-Pamies, O., 2021. The nonlinear viscoelastic response of suspensions of vacuous bubbles in rubber: I — Gaussian rubber with constant viscosity. *J. Elasticity*.
- Sidoroff, F., 1974. Un modèle viscoélastique non linéaire avec configuration intermédiaire. *J. de Mécanique* 13, 679–713.
- Simo, J.C., 1992. Algorithms for static and dynamic multiplicative plasticity that preserve the classical return mapping schemes of the infinitesimal theory. *Comput. Methods Appl. Mech. Engrg.* 99, 61–112.
- Stickel, J.J., Powell, R.L., 2005. Fluid mechanics and rheology of dense suspensions. *Annu. Rev. Fluid Mech.* 37, 129–149.
- Weir, C.E., 1951. Compressibility of natural and synthetic high polymers at high pressures. *J. Res. Natl. Bur. Stand.* 46 (207).
- Wood, L.A., Martin, G.M., 1964. Compressibility of natural rubber at pressures below 500 kg/cm<sup>2</sup>. *J. Res. Natl. Bur. Stand.* 68A, 259–268.
- Zener, C.M., 1948. *Elasticity and Anelasticity of Metals*. University of Chicago Press, Chicago.
- Ziegler, H., Wehrli, C., 1987. The derivation of constitutive relations from the free energy and the dissipation function. *Adv. Appl. Mech.* 25, 183–238.